Nonclassicality of Propagating States From 3-Photon Interactions in a Superconducting Parametric Cavity

by

Benjamin Jarvis-Frain

A thesis
presented to the University of Waterloo
in fulfilment of the
thesis requirement for the degree of
Master of Applied Science
in
Electrical and Computer Engineering (Quantum Information)

Waterloo, Ontario, Canada, 2024

Author's Declaration

I hereby declare that I am the sole author of this thesis. This is a true copy of the thesis, including any required final revisions, as accepted by my examiners.

I understand that my thesis may be made electronically available to the public.

Abstract

The multimode superconducting parametric cavity has proven to be a powerful and versatile system for producing nonclassical states of light in the microwave regime. Utilizing its ability to realize nonlinear and multimode Hamiltonians, we can produce strongly correlated propagating signals from the cavity at different frequencies including entangled photons. In this thesis, we study the generation of photon triplets using a cubic Hamiltonian in the cavity under a parametric drive.

We demonstrate the implementation of 3-photon Spontaneous Parametric Down-Conversion (SPDC) into different frequency modes of the cavity and study the non-Gaussian statistics of the outputted photon triplets through purely linear detection. We detail our methodology for performing absolutely calibrated measurements of the cavity output using a Shot Noise Tunnel Junction (SNTJ) as well as our use of a near quantum-limited Travelling-Wave Parametric Amplifier (TWPA). In addition to the primary results of this thesis, we present calibrated measurements of the noise temperature of the Crescendo TWPA from QuantWare.

Through the use of this TWPA and SNTJ, we are able to obtain the correlations between frequencies with low uncertainty up to the 4th moments. From these moments, we can compute a nonlinear entanglement witness on the propagating triplets and demonstrate the non-Gaussian genuine tripartite entanglement between photons with over 15 sigmas of certainty.

Acknowledgements

I would first like to express my sincerest gratitude to my supervisor, Christopher Wilson, for both taking me in to the Engineered Quantum System's Laboratory (EQSL) and for his support and mentorship in my endeavours throughout my degree. Chris's generous time investment to my instruction and thoughtful criticism of my work have been indispensable in my development as a researcher. His qualities as a physicist and engineer were both an invaluable resource and an example which I now strive to emulate. I would also like to thank the other members of my committee, Adrian Lupascu and Bradley Hauer, for their insightful comments on my thesis and many educational discussions throughout my degree.

It was my privilege to collaborate and learn from the senior researchers in the EQSL, especially Dima, Ibrahim, and Jamal. Dima's dedicated teaching and assistance in constructing cryogenic setups in the fridge was critical to my experiments as was the thoughtful wisdom that he often imparted. Ibrahim's extensive knowledge and unwavering support in fabricating my device was irreplaceable for this project, while his kindness and uplifting humor brought joy to the many long days and nights we spent in the cleanroom. Jamal offered me many illuminating insights into the physics of parametric interactions and superconducting devices which greatly deepened my understanding of my own experiments and the richness of this field.

Thank you to all of the other members of the EQSL, Andy, Bharat, Cindy, Gaung, Mohammad, and Richard, Zheng. Thank you as well to the many other researchers with whom I shared many interesting and engaging conversations Fernando, Sandbo, Amir, and Meg. My thanks especially to Sandbo whose pioneering research my own is a direct continuation of. And my sincere thanks to Andy, who contributed to many of the measurements described herein, for the sharp thinking and high energy that he brought to our collaborations.

Finally, I would like to thank everyone else who supported me through this journey. Thank you to my friends from back home and whom I made in Waterloo who provided many welcome distractions from the subject matter of this thesis. Thank you to my parents for their endless support and heartfelt encouragement, and to my brothers for consistently keeping my spirits high and my ego firmly on the ground. Lastly, thank you to my partner, Anna, whose patience, understanding, and love has made all of my achievements possible.

Table of Contents

List of Figures

List of Tables

Chapter 1

Introduction

In the last few decades the development and maturation of quantum technologies has enabled the control of quantum systems at an unprecedented level. These advances have lead to the realization of a plethora of quantum information experiments and applications with goals of useful quantum computing and quantum metrology now within sight [1, 2, 3]. At the frontier of this revolution are superconducting circuits [4, 5]. The compatibility of superconducting circuits with nanofabrication techniques and the nonlinearities offered by Josephson junctions have translated into an ability to create quantum systems at a large scale, with exotic behaviours, and even with programmable functionality.

The ability to engineer interactions between Josephson junctions and transmission lines or resonators has consequently lead to the emergence of the fields of microwave bosonic quantum information and microwave quantum optics. Using the vastly stronger nonlinearity of Josephson junctions than those available in the optical frequency, impressive experiments have been conducted measuring nonclassicality of microwave radiation through $g^{(2)}$ [6] and Wigner negativity [7], observing signatures of vacuum fluctuations through the dynamical Casimir effect [8], as well as demonstrating the generation of powerful states of light including GKP states [9] and cubic phase states [10].

1.1 Overview

In this thesis, we report on the generation of photon triplets from 3-photon spontaneous parametric down-conversion (SPDC) and for the first time, we have measured

entanglement witnesses observing its non-Gaussian genuine tripartite entanglement.

In chapter 2, an overview of superconductivity and superconducting circuits is presented beginning with the fundamental building blocks that constitute a DC superconducting quantum interference device (SQUID). This is built up to discussion of the circuit used to perform 3-photon SPDC, the parametric cavity. Included is an electromagnetic analysis of the cavity along with a detailed treatment of its Hamiltonian including how it can produce parametric 3-wave and 4-wave mixing processes necessary for 2-photon and 3-photon SPDC respectively.

In chapter 3, the experimental apparatus used to make these measurements is discussed with emphasis on the integration of a Crescendo Josephson travelling-wave parametric amplifier (TWPA) from QuantWare which was used to make low-noise measurements of the propagating states from the cavity. As an additional experiment to the main results of this thesis, the first noise temperature measurements made on a QuantWare Josephson TWPA are presented.

In chapter 4, the quantum information and quantum optics theory of our measurement scheme for obtaining operator expectation values and verifying genuine tripartite entanglement is presented. Included is theory of the method of moments where linear detection of a propagating amplified state's field is used to obtain operator expectations of a preamplified state, as well as discussion of how we translate voltage measurements from our electronics to field measurements of the propagating state. Furthermore, the anticipated non-Gaussian characteristics of the photon triplets are described along with a sufficient-but-not-necessary entanglement condition for verifying their non-Gaussian genuine tripartite entanglement.

Finally in chapter 5, experimental measurements of photon triplets are presented along with the first measurements of their violation of the entanglement witness described in chapter 4. A detailed error analysis of these measurements is also included to assess certainty of their nonclassicality.

Chapter 2

Superconducting Parametric Cavity Theory

The device of interest discussed in this thesis is a Coplanar Waveguide (CPW) resonator made from an aluminum thin film in the superconducting state on a silicon substrate. The resonator is terminated at one end by a capacitor coupling it to an input/output line and by a DC-SQUID at the other end which is flux driven by an external pump. In this chapter, the underlying physics of the constituent circuit elements will be discussed as well as the origin of parametric interactions.

2.1 BCS Superconductors

As is predicted by the Bardeen-Cooper-Schrieffer (BCS) model of superconductivity [11], the electrons in some elemental metals and compounds exhibit a weak attraction mediated by phonons in the bulk of the lattice. Below some critical temperature, this phonon-mediated interaction overpowers Coulombic repulsion leading to a net attractive interaction. This allows pairs of electrons to form bound states with energy below the Fermi level yielding an instability in the Fermi surface and the condensation of electrons into these paired states known as Cooper Pairs. The resulting condensate exhibits a macroscopic coherence and can be described by a collective wave function in terms of a Cooper pair density, n_c, and a macroscopic phase, θ [12]:

$$\psi(\mathbf{r},t) = \sqrt{n_c(\mathbf{r},t)}e^{i\theta(\mathbf{r},t)}. \tag{2.1}$$

This superconducting phase is not directly observable but it is central to the behaviours of Cooper pair supercurrents that arise in many physical systems. An expression for the relationship between the supercurrent density, macroscopic phase, and magnetic vector potential can be obtained from the theory of Ginzburg and Landau if we assume a Cooper pair density of the form of (2.1)

$$\mathbf{J} = \frac{n_c 2e}{m_c}(\hbar\nabla\theta - 2e\mathbf{A}), \tag{2.2}$$

where $2e$ and m_c are the charge and mass respectively of a Cooper pair, $\mathbf{J}$ is the supercurrent, and $\mathbf{A}$ is the magnetic vector potential [13]. Superconducting materials exhibit a variety of unique and useful properties such as the Meißner-Ochsenfeld effect [14] where magnetic fields are completely suppressed within the bulk by persistent current loops that form at the surface. This effect brings with it the corollary property and namesake of superconductors: that currents flow without internal dissipation. The approximate depth within which these persistent current loops flow and beyond which magnetic fields are entirely dispelled is the London penetration depth [15]:

$$\lambda_L = \sqrt{\frac{m_c}{\mu_0 n_c (2e)^2}}. \tag{2.3}$$

Since the magnetic vector potential has a gauge freedom where we can add to it the gradient of a scalar field, clearly the superconducting phase must have a similar freedom. We can nicely deal with these gauge freedoms in many circumstances by defining a gauge-invariant phase:

$$\gamma \equiv \oint \left(\nabla\theta - \frac{2e}{\hbar}\mathbf{A}\right) \cdot \mathrm{dl}. \tag{2.4}$$

2.2 Josephson Junctions

The fundamental building block of the circuit at the core of this thesis and indeed of most superconducting circuits is the Josephson Junction which is formed by two superconductors separated by a thin insulating barrier or some other weak link [17]. A voltage potential difference can exist across these weak links and in the case of an insulating barrier, quantum tunnelling of Cooper pairs enables the flow of a tunneling current. The relationship between this current and voltage is dependent on the difference in the gauge-invariant superconducting phases on either end of the junction, and is given by the Josephson relations

$$I = I_c \sin(\gamma) \tag{2.5}$$

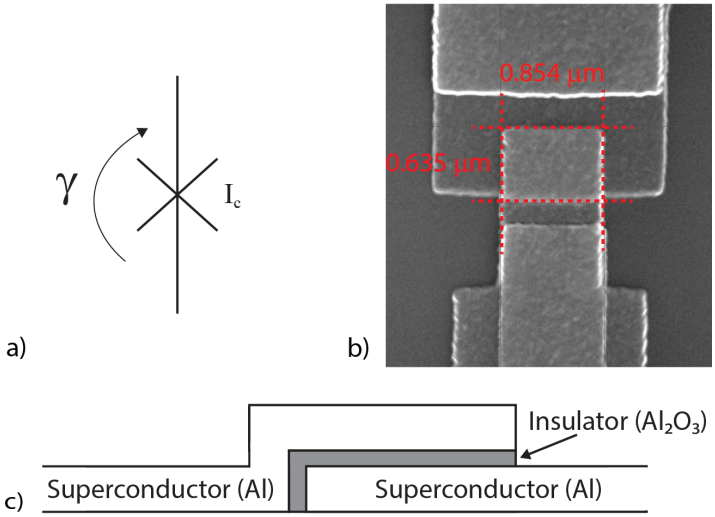

Figure 2.1: a) The circuit symbol for a Josephson junction with critical current I_c and a gauge-invariant phase γ across it. b) An SEM image of a Josephson junction used in the device described herein and fabricated using a Dolan-Bridge process [16]. The region denoted with red dashed lines is the area where two aluminum strips overlap and a junction is formed. c) A cartoon of a Josephson junction fabricated with evaporated aluminum films. The aluminum oxide provides the insulating barrier between the two aluminum superconductors which forms the junction.

$$V = \frac{\hbar}{2e}\dot{\gamma} \tag{2.6}$$

where I_c is the critical current which gives the maximum supercurrent that can flow through the junction. Through both of these relations, it can be seen that the gauge-invariant expression of the superconducting phase has an important effect on key observable quantities.

2.3 Flux Quantization

In the case of a volume of superconductor that is multiply connected, the equation for the supercurrent reveals a unique relationship between the superconducting phase and any applied magnetic flux. Consider a torus of superconductor and take a closed

contour integral over (2.2) around the torus as shown in figure 2.2:

$$\oint_C \mathbf{J} \cdot \mathrm{d}\mathbf{l} = \frac{n_c 2e}{m_c} \oint_C (\hbar \nabla \theta - 2e\mathbf{A}) \cdot \mathrm{d}\mathbf{l}.$$

Starting with the first term on the right hand side, we can use the fact that the integral of the gradient of a scalar function over some general contour is just the difference of the scalar at the two ends of the contour:

$$\int_{r_1}^{r_2} \nabla \theta \cdot \mathrm{d}\mathbf{l} = \theta_{r_2} - \theta_{r_1}.$$

We are interested in a closed contour where $r_1 = r_2$. However, θ_r is the phase of the wavefunction, $\psi(\mathbf{r})$ in equation (2.1) which must be singularly valued. Thus, this phase difference, $\theta_{r_2} - \theta_{r_1}$, must be zero modulo 2π and the second term on the right evaluates to

$$\hbar \oint_C \nabla \theta \cdot \mathrm{d}\mathbf{l} = 2\pi n \hbar$$

where n is any integer. Looking now at the second term on the right hand side, we can use the fact that the curl of the vector potential is the magnetic field along with Stoke's theorem which relates the line integral around C to the surface integral over the surface, S, enclosed by C to obtain:

$$-2e \oint_C \mathbf{A} \cdot \mathrm{d}\mathbf{l} = -2e \int_S \nabla \times \mathbf{A} \cdot \mathrm{d}s = -2e \int_S \mathbf{B} \cdot \mathrm{d}s.$$

And by definition, the integral of magnetic field over a surface is magnetic flux through the surface. We then obtain the following expression directly relating a phase shift along the loop to the current and flux through the loop:

$$\oint_C \mathbf{J} \cdot \mathrm{d}\mathbf{l} = \frac{n_c 2e}{m_c} (2\pi n \hbar - 2e \int_S \mathbf{B} \cdot \mathrm{d}s). \tag{2.7}$$

This equation should be true for any contour that we draw around the torus, and so we can use the Meißner-Ochsenfeld effect and choose a contour within the bulk of the superconductor where the screening current density must be 0. Along this contour the LHS is 0 yielding

$$2e \int_S \mathbf{B} \cdot \mathrm{d}s = 2\pi n \hbar.$$

We can see that the field integrated over the area of the loop must be exactly an integer multiple of some flux defined entirely using fundamental physical constants

$$\int_S \mathbf{B} \cdot \mathrm{d}s = n\frac{2\pi\hbar}{2e}$$

$$\Phi_{\text{ext}} = n\Phi_0 \tag{2.8}$$

where we can define $\Phi_0 \equiv \frac{h}{2e}$, which is called the magnetic flux quantum.

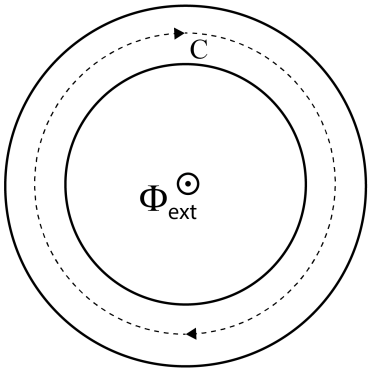

Figure 2.2: A superconducting torus threaded by an external flux Φ_{ext}. The contour of integration denoted C is inside the bulk of the superconductor beyond the depth λ_L

2.4 The DC-SQUID

The DC-SQUID is a circuit element made from a superconducting loop interrupted by two Josephson junctions and has proven to be an immensely useful and versatile element in the field of superconducting electronics [18, 19]. To understand its behaviour, we can extend the treatment of the supercurrent through a superconducting loop to a case with two junctions and two outgoing wires from the torus as shown in figure 2.3.

We can write down an expression for the phase along a close contour within the bulk of the torus that is analogous to (2.7) making the same assumption that we are far

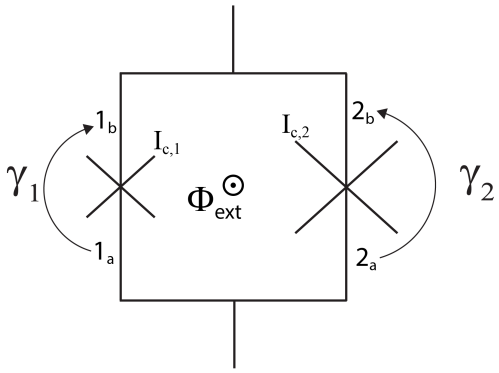

Figure 2.3: A DC-SQUID formed from a superconducting loop interrupted on each branch by Josephson junctions with critical currents $I_{c,1}$ and $I_{c,2}$. 1_a (2_a) and 1_b (2_b) denote the points in the superconducting loop immediately before and after the junction with current $I_{c,1}$ ($I_{c,2}$) . The flux Φ_{ext} threads the loop and alters the total current through the loop.

enough within the superconductor that the current density is effectively 0:

$$\frac{2e}{\hbar}\int_{2a}^{1a}\mathbf{A}\cdot\mathrm{d}\mathbf{l}=\int_{2a}^{1a}\nabla\theta\cdot\mathrm{d}\mathbf{l}$$
$$\frac{2e}{\hbar}\int_{1b}^{2b}\mathbf{A}\cdot\mathrm{d}\mathbf{l}=\int_{1b}^{2b}\nabla\theta\cdot\mathrm{d}\mathbf{l}.$$

Since the junctions themselves are not superconductors, we cannot naively apply the supercurrent equation over their region of the current, however, we can notice that that the expressions for the gauge-invariant phase across the junction give us the missing segments of the contour integrals:

$$\gamma_1+\frac{2e}{\hbar}\int_{1a}^{1b}\mathbf{A}\cdot\mathrm{d}\mathbf{l}=\int_{1a}^{1b}\nabla\theta\cdot\mathrm{d}\mathbf{l}$$
$$-\gamma_2+\frac{2e}{\hbar}\int_{2b}^{2a}\mathbf{A}\cdot\mathrm{d}\mathbf{l}=\int_{2b}^{2a}\nabla\theta\cdot\mathrm{d}\mathbf{l}.$$

If we now add the LHS and RHS of each of these expressions we get complete contour

integrals of $\nabla\theta$ and $\mathbf{A}$ over C:

$$\gamma_1 - \gamma_2 + \frac{2e}{\hbar}\oint_C \mathbf{A}\cdot \mathrm{d}\mathbf{l} = \oint_C \nabla\theta \cdot \mathrm{d}\mathbf{l}$$

$$\gamma_1 - \gamma_2 + 2\pi\frac{\Phi_{\text{ext}}}{\Phi_0} = 2\pi n. \tag{2.9}$$

Now that we have related the gauge-invariant phase to the flux threading the loop, we can consider its electrical behaviour. To better describe the behaviour of the SQUID, we can perform a change of variables in the phase to define a common mode phase and a differential mode phase. We will take the case of $n = 0$ and observe that the differential phase is directly proportional to the relative flux around the cavity:

$$\gamma_{\text{com}} = \frac{\gamma_2 + \gamma_1}{2} \tag{2.10a}$$

$$\gamma_{\text{diff}} = \frac{\gamma_2 - \gamma_1}{2}. \tag{2.10b}$$

We can consider the conserved common mode current entering and exiting the loop as the sum of the two currents through each junction:

$$\begin{aligned} I_{\text{SQ}} &= I_{c,1}\sin\gamma_1 + I_{c,2}\sin\gamma_2 \\ &= I_{c,1}\sin\left(\gamma_{\text{com}} - \gamma_{\text{diff}}\right) + I_{c,2}\sin\left(\gamma_{\text{com}} + \gamma_{\text{diff}}\right). \end{aligned}$$

Using the sum of angles identity, we obtain

$$\begin{aligned} I_{\text{SQ}} &= I_{c,1}\sin\gamma_{\text{com}}\cos\gamma_{\text{diff}} - I_{c,1}\cos\gamma_{\text{com}}\sin\gamma_{\text{diff}} \\ &\quad + I_{c,2}\sin\gamma_{\text{com}}\cos\gamma_{\text{diff}} + I_{c,2}\cos\gamma_{\text{com}}\sin\gamma_{\text{diff}} \\ &= (I_{c,1} + I_{c,2})\sin\gamma_{\text{com}}\cos\gamma_{\text{diff}} - (I_{c,1} - I_{c,2})\cos\gamma_{\text{com}}\sin\gamma_{\text{diff}}. \end{aligned}$$

Recognizing that the differential-mode phase is directly proportional to the externally applied flux from (2.10b) in the case $n = 0$, we can replace $\gamma_{\text{diff}} \to \pi\frac{\Phi_{\text{ext}}}{\Phi_0}$. The above current through the SQUID then varies as a function of both the externally applied flux as well as the common-mode gauge-invariant phase and in effect behaves as though it is itself a large Josephson junction with a flux-tunable critical current. It is thus reasonable to treat γ_{com} as the gauge-invariant phase difference across the entire SQUID and draw an analogous relationship to a flux across the SQUID, $\gamma_{\text{com}} \to 2\pi\frac{\Phi_{\text{SQ}}}{\Phi_0}$. We can then rewrite the SQUID current as

$$\begin{aligned} I_{\text{SQ}} = (I_{c,1} + I_{c,2})\sin\left(2\pi\frac{\Phi_{\text{SQ}}}{\Phi_0}\right)\cos\left(\pi\frac{\Phi_{\text{ext}}}{\Phi_0}\right) \\ - (I_{c,1} - I_{c,2})\cos\left(2\pi\frac{\Phi_{\text{SQ}}}{\Phi_0}\right)\sin\left(\pi\frac{\Phi_{\text{ext}}}{\Phi_0}\right). \end{aligned} \tag{2.11}$$

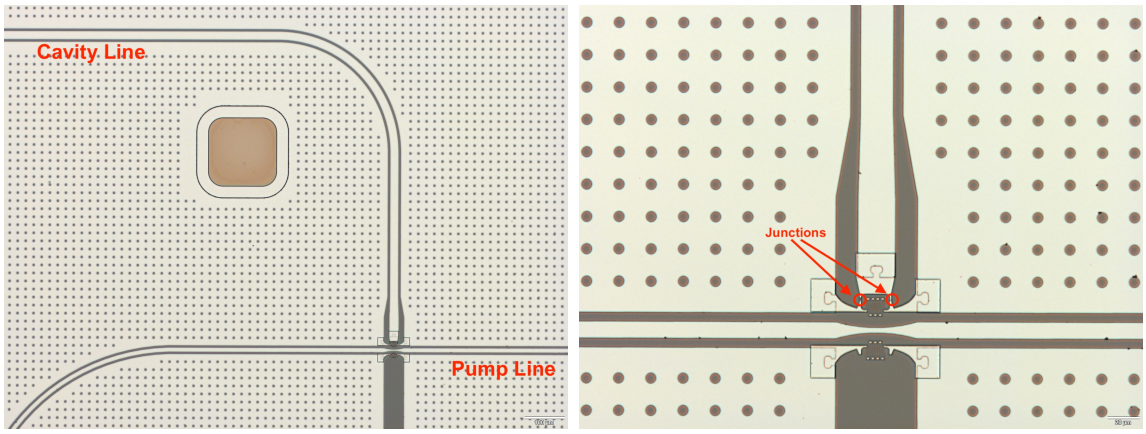

Figure 2.4: Micrographs of parametric cavity chip zoomed to region where the cavity line terminates with a SQUID coupled to a pump line at Left: 5x zoom Right: 20x zoom

The new critical current is simply the maximum value that (2.11) takes on over all Φ_{SQ} and is given by

$$I_{\text{SQ},c} = \sqrt{I_{c,1}^2 + I_{c,2}^2 + 2I_{c,1}I_{c,2}\cos\left(2\pi\frac{\Phi_{\text{ext}}}{\Phi_0}\right)}. \tag{2.12}$$

In the case where the two junctions in the SQUID are symmetric and $I_{c,1} = I_{c,2} \equiv I_c$, (2.11) simplifies to

$$I_{\text{SQ}} = 2I_c\cos\left(\pi\frac{\Phi_{\text{ext}}}{\Phi_0}\right)\sin\left(2\pi\frac{\Phi_{\text{SQ}}}{\Phi_0}\right). \tag{2.13}$$

2.5 CPW Cavities

The name parametric-cavity for this device is evocative of the cavities that have been used in the field of quantum optics for decades to study light-matter interactions in what is known as cavity quantum-electrodynamics [20]. However, the physical realization of this devices is actually entirely 2-dimensional and is formed from a Coplanar Waveguide (CPW) transmission-line terminated by a DC-SQUID enabling parametric interactions in the microwave regime. While it is possible to use 3-dimensional structures to study light-matter interactions with superconducting electronics [21], patterned 2D structures allow for fabrication of complex circuit geometries with relative ease and can potentially be made far more compact than 3D structures which

has important implications for potential scaling of quantum information experiments and devices.

2.5.1 Microwave Strategy

The microwave regime around 4-12 GHz is a preferable frequency range to operate superconducting quantum devices at as it has a high enough photon energy, $E = \hbar\omega$, that thermal photon populations are quite low at achievable operating temperatures. Additionally, it avoids the high cost of microwave electronics at frequencies in the K-bands (12-40 GHz) [22] and beyond.

CPW is a geometry of microwave transmission line consisting of a conducting strip centered between two ground planes patterned on a single side of a dielectric substrate [23]. The fact that the ground planes are symmetrically placed on either side of the center conductor leads to the propagating mode having a suppressed dipole moment and thus a decreased radiative loss. Moreover, the fact that the conductors in this device are made of superconducting films means that the high current densities that are characteristic of CPW do not contribute to propagation loss.

2.5.2 Impedance Boundary Reflections

A lossless transmission line can be modelled as a cascaded sequence of infinitesimal series inductors, L', and parallel capacitors, C', which gives rise to a wave equation that voltages and currents must obey [24]. The solutions to this wave equation are given as a superposition of forwards and backwards propagating waves that can be written as:

$$V(x,t) = V^+(x,t) + V^-(x,t) = V^+e^{-ikx} + V^-e^{ikx} \tag{2.14a}$$

$$\begin{aligned} I(x,t) = I^+(x,t) - I^-(x,t) &= I^+e^{-ikx} - I^-e^{ikx} \\ &= \frac{V^+}{Z_0}e^{-ikx} - \frac{V^-}{Z_0}e^{ikx} \end{aligned} \tag{2.14b}$$

Where the impedance of the line is $Z_0 = \sqrt{L'/C'}$. Any change in impedance either at a terminating load or at an abrupt change into another transmission line leads to a reflection in the propagating waves. This can be derived by the requirement for

continuity in $V(x,t)$ and $I(x,t)$ at the boundary $x_{1,2}$ from the initial impedance, Z_1, to the new impedance, Z_2:

$$V(x_{1,2}) = V_1^+ + V_1^- = V_2^+ + V_2^- \tag{2.15a}$$

$$I(x_{1,2}) = \frac{V_1^+ - V_1^-}{Z_1} = \frac{V_2^+ - V_2^-}{Z_2} \tag{2.15b}$$

If we consider an inputted forward travelling wave, V_1^+, and are interested in the partial reflection at this boundary, then we can set $V_2^- = 0$ and rearrange (2.15a) for the reflected wave, V_1^-. From this, we obtain the definition of the reflection coefficient, Γ:

$$V_1^- = V_1^+ \frac{Z_L - Z_0}{Z_L + Z_0} = V_1^+ \Gamma \tag{2.16}$$

2.5.3 Making a Cavity

By placing reflecting boundaries at either end of a transmission line, we can turn it into a cavity. The ideal SQUID is a nondissipative element and thus its purely imaginary impedance will always lead to perfect reflections. The SQUID junctions can be designed to have very large critical currents leading to a small inductance and a nearly short circuit termination [25]. At the other end of the cavity, the transmission line is coupled to an input/output line via a capacitor. By making the capacitance small, the impedance can be made quite large approximating an open circuit yielding the second reflecting boundary of the cavity.

It is possible to analyze this cavity entirely in terms of the reflection coefficient looking into the cavity which can give a strong understanding of interactions with incoming fields like parametric amplification. However, we are interested in spontaneous interactions with the vacuum fields inside the cavity and so it can be more instructive to analyze it from the perspective of modes inside the cavity.

With the same model of the transmission line as a cascade of infinitesmal inductors and capacitors over a length, d, we can derive its Hamiltonian to be

$$H = \int_0^d \left[\frac{1}{2C'} Q(x)^2 + \frac{1}{2L'} \left(\frac{\partial \Phi(x)}{\partial x} \right)^2 \right] \mathrm{d}x \tag{2.17}$$

where flux, Φ, and charge, Q, are both for an infinitesmal node in the cascade. Charge is thus defined per unit length as $Q = \int \frac{\partial I}{\partial x} \mathrm{d}t$ while flux is simply $\Phi = \int V \mathrm{d}t$ [26]. To find the boundary conditions for this system, we first consider the change in

transmission line current and voltage across infinitesimal series inductors and parallel capacitors respectively:

$$\frac{\partial V(x,t)}{\partial x} = V_{L'}(x,t) = L'\frac{\partial I(x,t)}{\partial t}$$
$$\frac{\partial I(x,t)}{\partial x} = I_{C'}(x,t) = C'\frac{\partial V(x,t)}{\partial t}.$$

Subsequently, we can integrate with respect to time to write the above expressions in terms of charge and flux across the infinitesmal capacitors and inductors respectively:

$$I(x,t) = \frac{1}{L'}\frac{\partial \Phi(x,t)}{\partial x} \tag{2.18}$$
$$V(x,t) = \frac{1}{C'}Q(x,t). \tag{2.19}$$

These equations now allow us to write down boundary conditions for flux and charge using the same current and voltage continuities that gave the definition of the reflection coefficient. In the case of our parametric cavity, the effectively open circuit coupling capacitor gives $I(d,t) = 0$ while the short circuit SQUID gives $V(0,t) = 0$.

To get a simple expression for just $\Phi(x,t)$, Hamilton's equations can give us an equation of motion where c is the speed of light in the cavity given by $c = 1/\sqrt{L'C'}$:

$$c^2\frac{\partial^2\Phi(x,t)}{\partial x^2} - \frac{\partial^2\Phi(x,t)}{\partial t^2} = 0. \tag{2.20}$$

Since we are only working with flux here, we can rewrite $V(0,t) = \partial\Phi(0,t)/\partial t = 0$ and then the solutions to equation (2.20) with the above boundary conditions are

$$\Phi(x,t) = \sum_{m=0}^{\infty} A_m \cos\left(2\pi\frac{x}{\lambda_m}\right)\sin(\omega_m t + \phi_m) \tag{2.21}$$
$$= \sum_{m=0}^{\infty} \Phi_m(x)\sin(\omega_m t + \phi_m)$$

subject to constraints that the wavelength is $\lambda_m = 4d/[2m+1]$ and the frequency is $\omega_m = 2\pi c/\lambda_m$. Since no initial conditions were defined, ϕ_m and A_m are free variables. Recognizing now that the equations of motion for this Hamiltonian are normal modes, we can rewrite it as a sum over these normal modes

$$H = \sum_{m=0}^{\infty}\left[\frac{1}{2C}Q_m^2 + \omega_m^2\frac{C}{2}\Phi_m^2\right] \tag{2.22}$$

where C is the total capacitance of the resonator.

2.5.4 Impedance Engineering

Clearly the resonances of the previously described cavity are evenly spaced in frequency which is problematic for performing parametric interactions which we will see is dependent on having unique differences between cavity modes. The solution to this problem is to engineer several abrupt changes in the impedance of the cavity along its length. This leads to partial reflections occurring within the cavity which alter the behaviour of its resonance modes. This can be viewed as effectively splitting the total cavity into N subcavities at points x_n. The subcavity modes are now strongly coupled by the previously derived boundary conditions applied to transitions between segments:

$$I_n(x_n,t) = I_{n+1}(x_n,t) \;\rightarrow\; \frac{1}{L'_n}\frac{\partial \Phi_n(x_n,t)}{\partial x} = \frac{1}{L'_{n+1}}\frac{\partial \Phi_{n+1}(x_n,t)}{\partial x} \tag{2.23a}$$

$$V_n(x_n,t) = V_{n+1}(x_n,t) \;\rightarrow\; \frac{1}{C'_n}Q_n(x_n,t) = \frac{1}{C'_{n+1}}Q_{n+1}(x_n,t). \tag{2.23b}$$

The resonances of each of these modes couple together creating a set of resonances for the entire cavity similar to the case with no impedance engineering. However, now the frequencies of each mode have been adjusted and are no longer evenly spaced in frequency as was intended. One other result of the impedance engineering is that the spacial modes $\Phi(x,t)$ and $Q(x,t)$ are no longer simply sinusoids over the entire cavity and so careful engineering of the impedance segments can be done to increase the participation ratio of key elements, namely the SQUID, with modes of the cavity.

The impedance engineering does not change the nature of the mode solutions to the wave equation, it only changes the form of $\Phi_m(x)$ which is now a piecewise set of sinusoids over the cavity. It also means that the effective capacitance seen by each mode can be different but that simply means that we must replace $C \rightarrow C_m$ in equation (2.22) which otherwise holds entirely true.

2.6 SQUID Mediated Parametric Interactions

We will finally now treat the behaviour of the SQUID termination to the transmission line and in doing so obtain a quantum description of the parametric interactions in the cavity. The Hamiltonian of the SQUID terminated cavity can simply be written as a sum of the transmission line Hamiltonian, (2.17), and the SQUID Hamiltonian which itself is computed from $H = \int I(t)V(t)\mathrm{d}t$. For completeness, we will also add a term for the flux pump's internal dynamics which will be relevant to the quantum

treatment:

$$\begin{aligned}
H &= H_{\mathrm{TL}} + H_{\mathrm{SQUID}} + H_{\mathrm{Pump}} \\
&= \sum_{m=0}^{\infty} \left[\frac{1}{2C_m} Q_m^2 + \omega_m^2 \frac{C_m}{2} \Phi_m^2 \right] + \int I_{\mathrm{SQ}}(\Phi_{\mathrm{SQ}}) \frac{\partial \Phi_{\mathrm{SQ}}}{\partial t} \mathrm{d}t + H_{\mathrm{Pump}} \\
&= \sum_{m=0}^{\infty} \left[\frac{1}{2C_m} Q_m^2 + \omega_m^2 \frac{C_m}{2} \Phi_m^2 \right] \\
&\qquad - 2\frac{I_c \Phi_0}{2\pi} \left| \cos\left(\pi \frac{\Phi_{\mathrm{ext}}}{\Phi_0} \right) \right| \cos\left(2\pi \frac{\Phi_{\mathrm{SQ}}}{\Phi_0} \right) + H_{\mathrm{Pump}}. \qquad (2.24)
\end{aligned}$$

Having now a Hamiltonian of the full system written entirely in terms of conjugate variables Φ and Q, we can promote these variables to operators $\hat{\Phi}$ and $\hat{Q}$ and subsequently perform a change of variables into annihilation and creation operators:

$$\hat{\Phi}_m = \sqrt{\frac{\hbar}{2\omega_m C_m}} (\hat{a}_m + \hat{a}_m^\dagger) \qquad (2.25a)$$

$$\hat{Q}_m = i\sqrt{\frac{\hbar \omega_m C_m}{2}} (\hat{a}_m - \hat{a}_m^\dagger) \qquad (2.25b)$$

We also express the external flux of a combination of a DC bias and the time-varying pump, $\Phi_e xt = \Phi_{\mathrm{DC}} + b_p \hat{\Phi}_p$ where b_p is a coupling constant relating the pump flux operator to the flux through the SQUID. This can similarly be treated with annihilation and creation operators which concisely describes its internal dynamics:

$$\hat{H} = \sum_{m=0}^{\infty} \hbar \omega_m \hat{a}_m^\dagger \hat{a}_m - 2\frac{I_c \Phi_0}{2\pi} \left| \cos\left(\pi \frac{\Phi_{\mathrm{DC}} + b_p \hat{\Phi}_p}{\Phi_0} \right) \right| \cos\left(2\pi \frac{\hat{\Phi}_{\mathrm{SQ}}}{\Phi_0} \right) + \hbar \omega_p \hat{a}_p^\dagger \hat{a}_p.$$

Since the SQUID terminates the cavity, $\Phi_{\mathrm{SQ}} = \Phi(d, t)$, we can write $\hat{\Phi}_{\mathrm{SQ}}$ as a sum of $\hat{\Phi}_m$ mediated by the coupling constants, b_m, of the SQUID in each mode flux: $\hat{\Phi}_{\mathrm{SQ}} = \sum_m b_m \hat{\Phi}_m$. We are interested in circumstances where the cavity is populated by just a few photons and so we can very reasonably expand the cosine of SQUID flux, $\hat{\Phi}_{\mathrm{SQ}}$, to lowest order about 0. Finally, we can expand the pump cosine to lowest order − which is linear for nonzero Φ_{DC} − and collect all of these expansion factors into g'

$$\hat{H} = \sum_{m=0}^{\infty} \hbar \omega_m \hat{a}_m^\dagger \hat{a}_m + \hbar \omega_p \hat{a}_p^\dagger \hat{a}_p - \hbar g' (\hat{a} + \hat{a}_p^\dagger) \left[\sum_{m=0}^{\infty} \sqrt{\frac{b_m^2 \hbar}{2\omega_m C_m}} (\hat{a}_m + \hat{a}_m^\dagger) \right]^2 \qquad (2.26a)$$

$$g' \equiv \frac{2\pi^2 I_c}{\hbar \Phi_0^2} \frac{\Phi_{\mathrm{DC}}}{\Phi_0} \sqrt{\frac{b_p^2 \hbar}{2\omega_p C_p}} \qquad (2.26b)$$

where we have dropped terms that are 0th or 2nd order in $\hat{\Phi}_p$. We now have a quantum Hamiltonian of the linear pump and cavity modes along with a three-wave mixing process between each of them resulting from the SQUID termination. If we group together each mode's internal dynamics into the fully time-independent Hamiltonian:

$$\hat{H}_0 = \sum_{m=0}^{\infty} \hbar\omega_m \hat{a}_m^\dagger \hat{a}_m + \hbar\omega_p \hat{a}_p^\dagger \hat{a}_p. \tag{2.27}$$

Going into the interaction picture using $\hat{U}_0 = \exp(i\hat{H}_0 t/\hbar)$ the coupling term in the Hamiltonian becomes

$$\begin{aligned}
&\hat{H}_{\mathrm{SQ}}^{(I)} \\
&= \hat{U}_0 \hat{H}_{\mathrm{SQ}} \hat{U}_0^\dagger \\
&= \hbar g'(\hat{a}_p e^{-i\omega_p t} + \hat{a}_p^\dagger e^{i\omega_p t}) \left[\sum_{m=0}^{\infty} \sqrt{\frac{b_m^2 \hbar}{2\omega_m C_m}} (\hat{a}_m e^{-i\omega_m t} + \hat{a}_m^\dagger e^{i\omega_m t})\right]^2 \\
&= \hbar g'(\hat{a}_p e^{-i\omega_p t} + \hat{a}_p^\dagger e^{i\omega_p t}) \times \\
&\sum_{m=0}^{\infty}\sum_{n=0}^{\infty} \sqrt{\frac{b_m^2 \hbar}{2\omega_m C_m}} \sqrt{\frac{b_n^2 \hbar}{2\omega_n C_n}} \left[\hat{a}_m \hat{a}_n e^{-i(\omega_m+\omega_n)t} + \hat{a}_m^\dagger \hat{a}_n e^{i(\omega_m-\omega_n)t}\right. \\
&\qquad \left. + \hat{a}_m \hat{a}_n^\dagger e^{i(\omega_n-\omega_m)t} + \hat{a}_m^\dagger \hat{a}_n^\dagger e^{i(\omega_m+\omega_n)t}\right].
\end{aligned} \tag{2.28}$$

By carefully selecting the pump frequency, ω_p, we can choose which terms will be static in the interaction picture and which will be rotating. The frequency of the rotating terms will be on the order of GHz and so we can apply the rotating-wave approximation which supposes that they will average to zero over many periods of rotation.

As one example of this process we can consider the case of $\omega_p = 2\omega_1$ which yields a squeezing operation on mode 1:

$$\begin{aligned}
\hat{H}_{2\omega_1}^{(I)} &= \hbar g' p_1^2 (\hat{a}_p e^{-i2\omega_1 t} + \hat{a}_p^\dagger e^{i2\omega_1 t}) \left[\hat{a}_1 \hat{a}_1 e^{-i2\omega_1 t} + \hat{a}_1^\dagger \hat{a}_1 + \hat{a}_1 \hat{a}_1^\dagger + \hat{a}_1^\dagger \hat{a}_1^\dagger e^{i2\omega_1 t}\right] + \hat{H}_{\mathrm{Rot}}(t) \\
&= \hbar g_{11} (\hat{a}_p \hat{a}_1^\dagger \hat{a}_1^\dagger + \hat{a}_p^\dagger \hat{a}_1 \hat{a}_1) + \hat{H}_{\mathrm{Rot}}(t) \\
&\approx \hbar g_{11} (\alpha_p \hat{a}_1^\dagger \hat{a}_1^\dagger + \alpha_p^* \hat{a}_1 \hat{a}_1)
\end{aligned} \tag{2.29}$$

We have replaced $g' p_1^2$ with an overall coupling constant for this interaction, g_{11}, and in the final step we have applied the aforementioned rotating-wave approximation where we drop $\hat{H}_{\mathrm{Rot}}(t)$. We have also made the parametric approximation in which we assume that the pump mode is populated by a coherent state with a macroscopically large amplitude such that the pump operators, $\hat{a}_p$, can be treated as scalars, α_p.

By selecting pump frequencies that are equal to sums and differences between cavity modes we can produce a variety of 2-photon interactions inside the cavity.

2.7 Extending SQUID mediated interactions to 3rd-Order

Critically, the Hamiltonian of the symmetric SQUID can only produce even order terms in $\hat{a}$ and $\hat{a}^\dagger$ since cosine is an even function. If we were to expand it to higher order, the next nonzero term would be fourth order and so clearly symmetric SQUID terminations are incapable of producing 3-photon cavity interactions. To see how we can obtain a cubic Hamiltonian, we need to consider the Hamiltonian of a SQUID made from Josephson junctions of different critical currents. Returning to the current through an asymmetric SQUID (2.11) we obtain its Hamiltonian as:

$$H_{\mathrm{SQ}} = -E_{J+}\cos\left(\pi\frac{\Phi_{\mathrm{ext}}}{\Phi_0}\right)\cos\left(2\pi\frac{\Phi_{\mathrm{SQ}}}{\Phi_0}\right) - E_{J-}\sin\left(\pi\frac{\Phi_{\mathrm{ext}}}{\Phi_0}\right)\sin\left(2\pi\frac{\Phi_{\mathrm{SQ}}}{\Phi_0}\right) \tag{2.30}$$

. With $E_{J+} = \frac{\Phi_0}{2\pi}(I_{c,1} + I_{c,2})$ and $E_{J-} = \frac{\Phi_0}{2\pi}(I_{c,1} - I_{c,2})$. The above expression can be approximated as follows revealing an effective bias term in the cavity flux cosine:

$$\alpha(\hat{\Phi}_{\mathrm{ext}}) = \arctan\left[\tan\left(\pi\frac{\hat{\Phi}_{\mathrm{ext}}}{\Phi_0}\right)\frac{E_{J-}}{E_{J+}}\right] \tag{2.31}$$

$$\hat{H}_{\mathrm{SQ}} \approx (E_{J+} + E_{J-})\sqrt{1 - 2\frac{E_{J-}}{E_{J+}}}\left|\cos\left(\pi\frac{\hat{\Phi}_{\mathrm{ext}}}{\Phi_0}\right)\right|\cos\left[2\pi\frac{\hat{\Phi}_{\mathrm{SQ}}}{\Phi_0} - \alpha(\hat{\Phi}_{\mathrm{ext}})\right] \tag{2.32}$$

Considering the external flux as a DC component and an RF perturbation, $\hat{\Phi}_{\mathrm{ext}} = \Phi_{\mathrm{DC}} + \lambda\hat{\Phi}_p$, the bias term can itself be written as $\alpha(\hat{\Phi}_{\mathrm{ext}}) \approx \alpha_0(\Phi_{\mathrm{DC}}) + \lambda\alpha_1(\hat{\Phi}_{\mathrm{p}})$. One may suppose that the existence of a DC bias in the cavity flux cosine suggests that a cavity interacting with an asymmetric SQUID natively supports cubic interactions, that is, 3-photon interactions exist between cavity modes even in the absence of a parametric pump. However, this is false since an expansion in powers of $\hat{\Phi}_{\mathrm{SQ}}$ must always be done about a minimum of the Hamiltonian, and $\hat{\Phi}_{\mathrm{SQ}}$ can simply take on a DC offset in order to reach this minimum [27]. We can observe this transformation

as follows:

$$\hat{\Phi}_{\mathrm{SQ}} \rightarrow \hat{\Phi}_{\mathrm{SQ}} + \frac{\Phi_0}{2\pi}\alpha_0(\Phi_{\mathrm{DC}}) \tag{2.33}$$

$$\hat{H}_{\mathrm{SQ}} \rightarrow (E_{J+} + E_{J-})\sqrt{1 - 2\frac{E_{J-}}{E_{J+}}} \times \left|\cos\left(\pi\frac{\Phi_{\mathrm{DC}} + \lambda\hat{\Phi}_p}{\Phi_0}\right)\right| \cos\left[2\pi\frac{\hat{\Phi}_{\mathrm{SQ}}}{\Phi_0} - \lambda\alpha_1\left(\hat{\Phi}_{\mathrm{p}}\right)\right]. \tag{2.34}$$

This transformation of the cavity flux is the exact same reason why the Hamiltonian of a symmetric SQUID (2.30) is expressed with absolute signs around the external flux cosine. When the external flux causes the sign of the cosine to flip, this simply means the minimum has shifted by $\Phi_0/2$ in Φ_{SQ} in which case a transformation like (2.33) will occur restoring the sign.

Finally, we can expand equation (2.34) to 1st order in λ and convert flux operators into annihilation and creation operators which will now give us terms with all powers of $\hat{a}$ and $\hat{a}^\dagger$. We can again collect expansion coefficients along with participation ratio coefficients to obtain overall coupling coefficients. Looking in the interaction picture, the 3rd-order terms in our SQUID Hamiltonian will be of the form

$$\hat{H}^{(I)}_{\mathrm{SQ},\,3} = \hbar(\hat{a}_p e^{-i\omega_p t} + \hat{a}_p^\dagger e^{i\omega_p t})\times \sum_{l,m,n}^{\infty} g_{lmn}(\hat{a}_l e^{-i\omega_l t} + \hat{a}_l^\dagger e^{i\omega_l t})(\hat{a}_m e^{-i\omega_m t} + \hat{a}_m^\dagger e^{i\omega_m t})(\hat{a}_n e^{-i\omega_n t} + \hat{a}_n^\dagger e^{i\omega_n t}) \tag{2.35}$$

with g_{lmn} analogous to g' in 2.26b though also now including constants for modes l, n, m. If we consider the case of pumping at $\omega_p = \omega_1 + \omega_2 + \omega_3$, then we will obtain the following Hamiltonian after the rotating-wave and parametric approximations:

$$\hat{H}^{(I)}_{\omega_1+\omega_2+\omega_3} \approx \hbar g_{123}(\alpha_p \hat{a}_1^\dagger \hat{a}_2^\dagger \hat{a}_3^\dagger + \alpha_p^* \hat{a}_1 \hat{a}_2 \hat{a}_3). \tag{2.36}$$

This Hamiltonian corresponds to 3-photon spontaneous parametric down-conversion which enables the production of triplets of daughter photons. Similarly it can be viewed as a generalized form of squeezing where the correlations are generated across 3 modes instead of 2 and thus is called Trisqueezing [27]. The propagating states emitted from the parametric cavity while it performs this Hamiltonian are the primary subject of the experiments in this thesis.

Chapter 3

Low-Noise Measurements of Propagating States

This chapter is largely concerned with the techniques and systems used to perform calibrated low-noise measurements of propagating states radiating from the cavity. Chapter 3.5 describes an experiment performed to measure the noise temperature and gain of a commercial parametric amplifier from QuantWare.

The photon flux in the states of interest are only a few photons/s/Hz and so the population of thermal photons in the cavities environment must be exceptionally low. Moreover, they must be greatly amplified before leaving the low temperature environment in order to be detectable over the background at room temperature. This must be done using an amplification chain with several orders of magnitude of gain and yet a low enough added noise level to not overpower the signal emitted from the cavity.

These challenges of detecting the signal amidst thermal and amplification noise are overcome by conducting the experiment in an exceptionally low temperature environment and using a near-quantum limited parametric amplifier as the first amplification stage before moving on to a low-noise transistor based amplification chain.

Finally, we must be able to relate the amplified signal detected at room temperature back to the state emitted from the cavity which requires an absolute calibration of the gain and noise temperature of the amplification chain. This is done using a shot-noise tunnel junction which acts as a self-calibrated noise source.

3.1 Parametric Amplification

Since this experiment depends on the ability to accurately measure extremely weak signals, an amplifier with a noise power approaching the limit of what quantum mechanics permits is necessary to perform these measurements with low uncertainty.

3.1.1 Noise Temperature

The noise added to the signal after it leaves the cavity can be quantified using noise temperature. Noise temperature, T_N, describes the power of the added noise, N_0, in terms of the temperature at which a matched source would need to be to produce N_0 through Johnson-Nyquist noise using the Rayleigh-Jeans approximation [24]. This relationship is given by

$$N_0 = k_B T_N B. \tag{3.1}$$

Where k_B is Boltzmann's constant, and B is the bandwidth of interest. In the case of an amplifier, noise temperature is defined such that the equivalent noise source is placed at the input of the amplifier and so the total power output including noise, N, and signal, S, from an amplifier with noise temperature ,T_N, and gain, G, is

$$S_{\text{Out}} + N_{\text{Out}} = G(S_{\text{In}} + k_B T_N B). \tag{3.2}$$

We can then define the total noise temperature for a cascaded chain of M amplifiers with noise temperatures, $T_{N,i}$ and gains G_i to be [24]

$$T_{N,\text{Total}} = T_{N,0} + \sum_{i=1}^{M} \frac{T_{N,i}}{\prod_{j=0}^{i-1} G_j}. \tag{3.3}$$

In many cases, the gain of an amplification stage is much larger than the difference in noise temperature between stages, $T_{N,i+1} \ll G_i \times T_{N,i}$, and so the noise temperature of the entire amplification chain is dominated by the temperature of just the first stage. For this reason, it is critical that the first amplification state has as low a noise temperature as possible which is bounded by the standard quantum limit.

3.1.2 The Standard Quantum Limit

Since we wish to measure both quadratures and thus also the phase information of the signals emitted by the cavity, the amplifiers used in the measurement chain

must be phase-insensitive which means that parametric amplification must be done in a nondegenerate operating mode. Nondegenerate parametric amplification can be viewed as effectively a two-mode squeezing operation between a signal mode and an idler mode which adds to the signal mode a minimum number of noise photons, A, given by [28, 29, 30]

$$A \geq \frac{1}{2}\left|1 - \frac{1}{G}\right|. \tag{3.4}$$

This can easily be converted to a minimum noise temperature by considering the energy of a photon, $E = hf$, and comparing it with the thermal energy for some temperature [31, 32]:

$$T_N \geq \frac{hf}{2k_B}\left|1 - \frac{1}{G}\right|. \tag{3.5}$$

3.1.3 Travelling-Wave Parametric Amplifiers

In the experiments described in this thesis, correlations between cavity output signals at multiple frequencies had to be measured which necessitated the use of an amplification chain with an instantaneous bandwidth of several GHz. This rules out the use of resonator parametric amplifiers and so the solution is to use a Josephson Travelling-Wave Parametric Amplifier (TWPA). We use the Crescendo TWPA made by QuantWare.

A TWPA is a metamaterial transmission line made of repeated unit cells that are each a resonant circuit with some nonlinear component. The signal travels down the transmission line along with a strong pump tone and parametric amplification is performed in each cell along the length of the line. The TWPA used in these experiments utilizes four-wave mixing and so the frequencies of the pump (ω_p), signal (ω_s), and idler (ω_i) tone must all obey the energy conservation condition for four-wave parametric amplification:

$$2\omega_p = \omega_i + \omega_s. \tag{3.6}$$

Furthermore, the phase relationship between the three tones must be preserved as they travel along the waveguide which applies a constraint on the wave numbers, k_p, k_s, k_i, analogous to conservation of momentum and not present in resonator parametric amplifiers:

$$2k_p - k_i - k_s = 0. \tag{3.7}$$

While (3.6) alone can always be satisfied by the spontaneous generation of an idler tone, the ability for a generated idler to simultaneously satisfy (3.6) and (3.7) is dependent on the dispersion relation $k(\omega)$ of the metamaterial. In the TWPA used

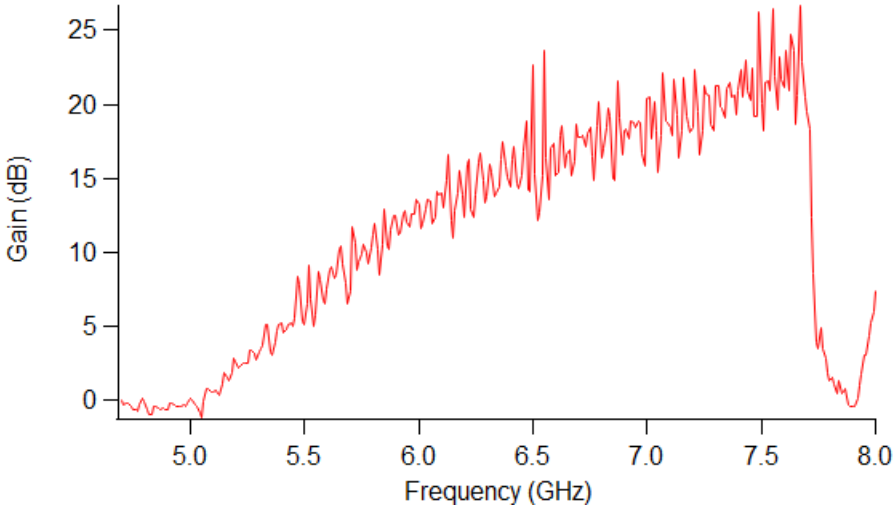

Figure 3.1: The gain of the TWPA measured using the techniques described in chapter 3.5 and used in the experiments described in chapter 5. The drop in gain seen near 7.7 GHz is due to the presence of the dispersive feature.

for these experiments, the dispersion relation has been engineered with the addition of passive resonant structures along with the nonlinear unit cells to ensure (3.6) and (3.7) can be satisfied simultaneously enabling high gain over a large band. This is done at the cost of introducing a stopband into the middle of the gain band known as the dispersive feature.

3.2 Dilution Refrigerator and Microwave Network

The low temperature environment in which these experiments take place is at the mixing chamber stage of a dilution refrigerator, cooled to roughly 10 mK in a setup depicted in Figure 3.2. The stages of the fridge are all housed inside a vacuum can pumped down to high-vacuum and are outfitted with a matryoshka of shielding around the highest temperature stage and between stages. This isolates the experiment at the mixing chamber stage from both radiative heat and electromagnetic noise. In addition to Johnson-Nyquist noise at room temperature, microwave signals from wireless communications and power cables for instruments and dilution fridge equipment can all produce powerful interference which necessitate strong shielding and attenuation on lines routing to the experiment.

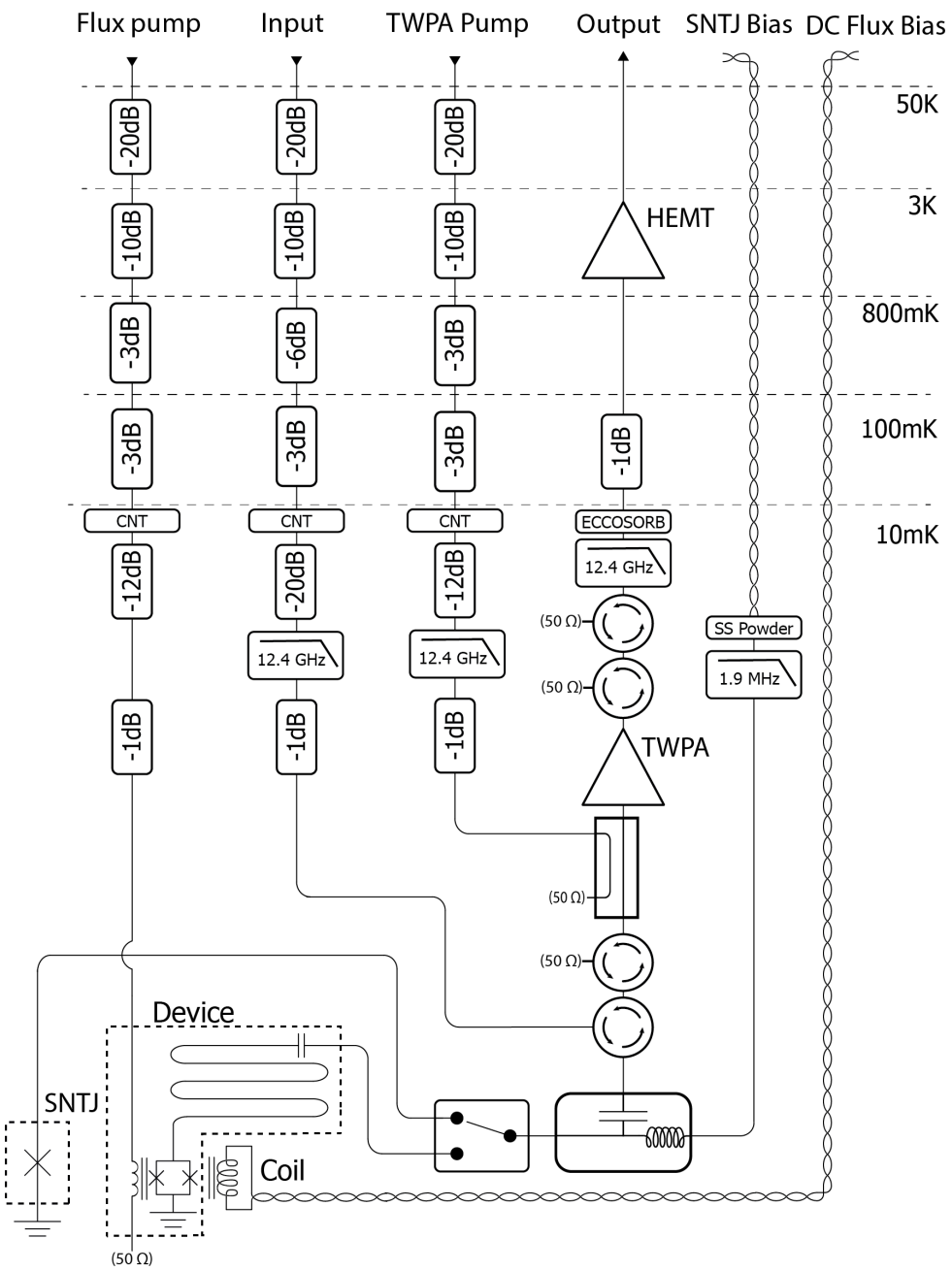

Figure 3.2: Schematic of microwave network inside the dilution refrigerator used to measure propagating states emitted from the parametric cavity as described in chapter 5. The resistive network used to set the bias voltage on the SNTJ is omitted for space (shown on figure 3.4.)

Signals are routed from room temperature to the experiment using microwave coaxial cables with several orders of magnitude of attenuation distributed over the multiple temperature stages of the fridge. Commercial lowpass filters suppress noise signals at frequencies just above experimental bands while bespoke filters made from a mixture of stainless steel and Carbon Nanotube (CNT) powder acting as lowpass filters provide strong suppression far above the experimental bands [33]. The output line lacks such attenuation as it would enormously degrade the gain of the amplification chain and thus also the effective noise temperature. Instead, isolation from external noise is achieved using circulators which nonreciprocally transmit outbound signals from the fridge while routing inbound signals into 50 Ω loads. These loads are themselves thermalized to the low temperature stages and thus introduce relatively low thermal noise. Since the CNT filters are fairly lossy towards the upper end of the experimental band, a commercial eccosorb filter was introduced for later experiments to play the same role as the CNT filters on the output line.

Since the TWPA is a parametric amplifier, its ability to produce gain is dependent on the presence of a strong parametric pump tone to activate the four-wave mixing processes. This pump tone is roughly 40 dB larger than the largest signal strength that we would want to allow into the parametric cavity before we might expect it to produce nonlinearities that would disrupt the experiment. Thus, the setup must have very strong isolation between the pump and cavity. To achieve this, a directional coupler with high isolation is used to initially couple the pump tone into the TWPA input and an additional pair of circulators is placed in between the directional coupler and the cavity to achieve the more than 40 dB isolation needed.

An additional challenge when integrating a TWPA into a measurement setup is oscillations than can occur if poorly matched components form an effective resonator around the TWPA. The solution is to ensure the input and output of the TWPA see a perfectly matched 50 Ω environment over its entire amplification band which can be challenging since its amplification band is several GHz. In this setup broadband matching was achieved using the same broadband circulators mentioned earlier for output line and parametric pump isolation.

The amplification chain used for these experiments starts with a TWPA which provides an exceptionally low-noise initial amplification stage while a sequence of transistor based low-noise amplifiers are used to achieve the nearly 100 dB gain that is needed to bring the signal from the few photon regime to a power level that can be measured by room temperature instruments. The first amplifier following the TWPA is a High Electron Mobility Transistor (HEMT) amplifier which provides over 30 dB of gain across our measurement band with a noise temperature around 5 K. The rest of the amplification chain is outside the fridge at room temperature with each tran-

sistor having a noise temperature around 300 K. From equation (3.3) we can then see that the noise temperature of each stage after the HEMT has a negligible contribution to the total noise temperature of the chain. The significance of the HEMT's contribution itself is dependent on the operating gain and noise of the TWPA and creates a key trade-off when selecting an operating point of the TWPA.

3.3 Shot Noise Tunnel Junction as a Self-Calibrated Source

To be able to relate signals measured at room temperature to the signals outputted from the cavity, we must know the total gain and loss experienced by the signals along the chain. This requires us to be able to pass a signal of a precisely known power into the same amplification chain used for the cavity signals. In these experiments, it is done using a Shot-Noise Tunnel Junction (SNTJ) provided by the National Institute of Standards and Technology (NIST) [34, 35, 36]. The SNTJ consists of an insulating barrier between two normal-metal electrodes forming a 50 Ω tunneling junction that is matched to the transmission line. The SNTJ used in this experiment is an aluminum junction forced into the normal-metal state by a strong rare-earth magnet even at 10 mK. When exposed to a DC bias voltage, electrons will tunnel across the junction producing shot noise with a broadband noise power that can be accurately predicted as a function of voltage and physical temperature. For any given frequency band, the junction will also produce quantum Johnson-Nyquist noise as must be the case for any circuit element and these noise sources combine together with the gain and noise temperature of the measurement chain to produce a cumulative observed noise power. This observed noise power is given by the following expression assuming that the junction is perfectly matched to the amplification chain and that the power is measured over a sufficiently narrow bandwidth such that the frequency can be treated as constant [37]:

$$P_{\mathrm{SNTJ}} = G \cdot B \cdot k_B \left[T_N + \frac{eV + hf}{4k_B} \coth\left(\frac{eV + hf}{2k_B T}\right) + \frac{eV - hf}{4k_B} \coth\left(\frac{eV - hf}{2k_B T}\right) \right]. \tag{3.8}$$

Figure 3.3 shows an example noise power output as a function of applied DC voltage when measuring the noise of the amplification chain without the TWPA. Equation (3.8) is fit to the data collected and the parameters of the amplifier chain are obtained

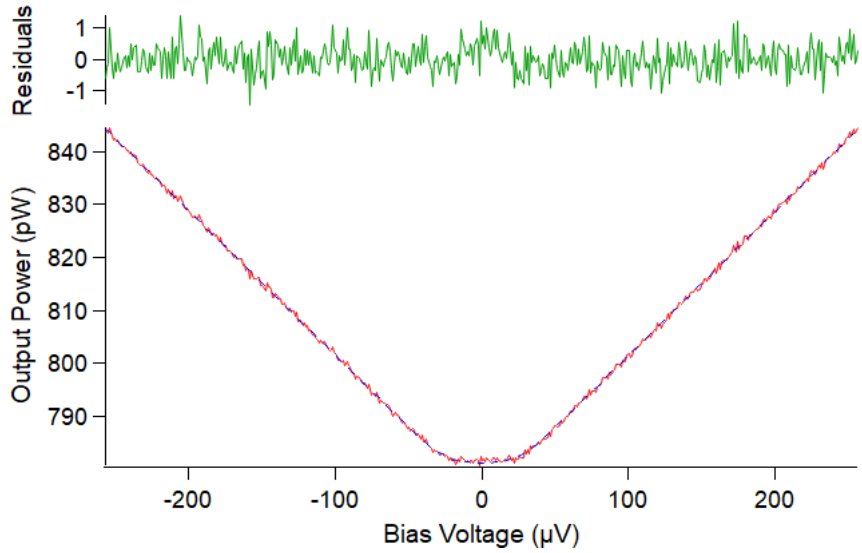

Figure 3.3: SNTJ output noise power (red) measured through HEMT amplification chain and fitted (blue) with residuals (green) to characterize the gain and noise temperature of the TWPA. The noise temperature in the region near 0 V bias where the power is constant with respect to voltage is dominated by quantum noise given by $T_n = hf/2k_B$. In this TWPA characterization experiment, $f = 6.02$ GHz, $G = 65.3$ dB, $T_N = 16.37$ K, and $T = 63$ mK.

from the parameters found by the fit. While gain is the only property necessary to be able to reconstruct the propagating cavity states from room temperature measurements, the noise temperature can be used as an indication of the performance of the measurement system while the junction temperature can be used to give confidence to the assumptions that thermal photon populations in the cavity are low. Furthermore, knowing the noise temperature of the amplification chain is critical to performing noise temperature measurements of components not included in the amplification chain as will be described in chapter 3.5.

3.4 Superheterodyne measurement

The instruments used to measure signals emitted from the cavity at room temperature and convert them to digital waveforms are Aeroflex 3025 and 3036 digitizer modules which use local oscillator (LO) tones to mix down incoming signals to an intermediate frequency (IF) at 187.5 MHz, where it can then digitize the signal. By mixing down

the signal before sampling it, a relatively low sample-rate Analog to Digital Converter (ADC) can be used to digitize frequencies over a variable band up to several GHz. However, it has a drawback in that it is also mixing down signals at $2 \times f_{\mathrm{IF}} = 375$ MHz above or below the intended band into the same IF frequency. This is a result of the fact that mixing produces new frequencies at $f_{\mathrm{IF}} = f_{\mathrm{S}} \pm f_{\mathrm{LO}}$. In the case of a high-side injection where we set f_{LO} such that $f_{\mathrm{S}} = f_{\mathrm{LO}} - 187.5$ MHz, we will also be mixing down any signal satisfying $f_{\mathrm{Im}} = f_{\mathrm{LO}} + 187.5$ MHz to the same IF. We call this unwanted down-converted band the image band.

The presence of an image band causes issues since our experiments rely on measuring noise statistics and yet naively digitizing the signal will result in us measuring the combined noise of the intended band and image band. One solution to this issue is to design filters that will pass exactly the intended signal frequency while strongly supressing the image band above or below the signal. This can be a straightforward approach but it requires a bespoke filter to be made at each frequency of interest which may not be known prior to the cooldown and is completely infeasible if a measurement is to be made over a broad band of frequencies. Furthermore, the designed filters must have a relatively high quality-factor since they need to have a strong roll-off over a few hundred MHz despite having a passband at several GHz. An alternative solution which was used in this thesis is to build and utilize a superheterodyne setup.

Superheterodyne adds an additional mixing step to the measurement process with an extra initial IF. Before entering the digitizer, the signal is mixed down to a superheterodyne IF, $f_{\mathrm{IF,SH}}$, of a few GHz where a sharp cutoff filter then suppresses the image band. This solution solves the two major issues with using image rejection filters directly on the signal. With a variable frequency superheterodyne LO, it is relatively easy to sweep the signal frequency being mixed into $f_{\mathrm{IF,SH}}$ and only a single filter is needed to suppress the image band at $f_{\mathrm{IF,SH}}$ for a wide range of signal frequencies. Furthermore, since $f_{\mathrm{IF,SH}}$ is much lower than f_{S}, the filter used for image band suppression can have a lower quality factor. Of course, an additional step of mixing produces its own new image band. However, since $f_{\mathrm{Im}} = f_{\mathrm{S}} + 2 \times f_{\mathrm{IF,SH}}$ and $f_{\mathrm{IF,SH}}$ is a few GHz, this image band is several GHz above the signal band and a single low quality-factor filter can be used to suppress this new image band over a wide range of frequencies.

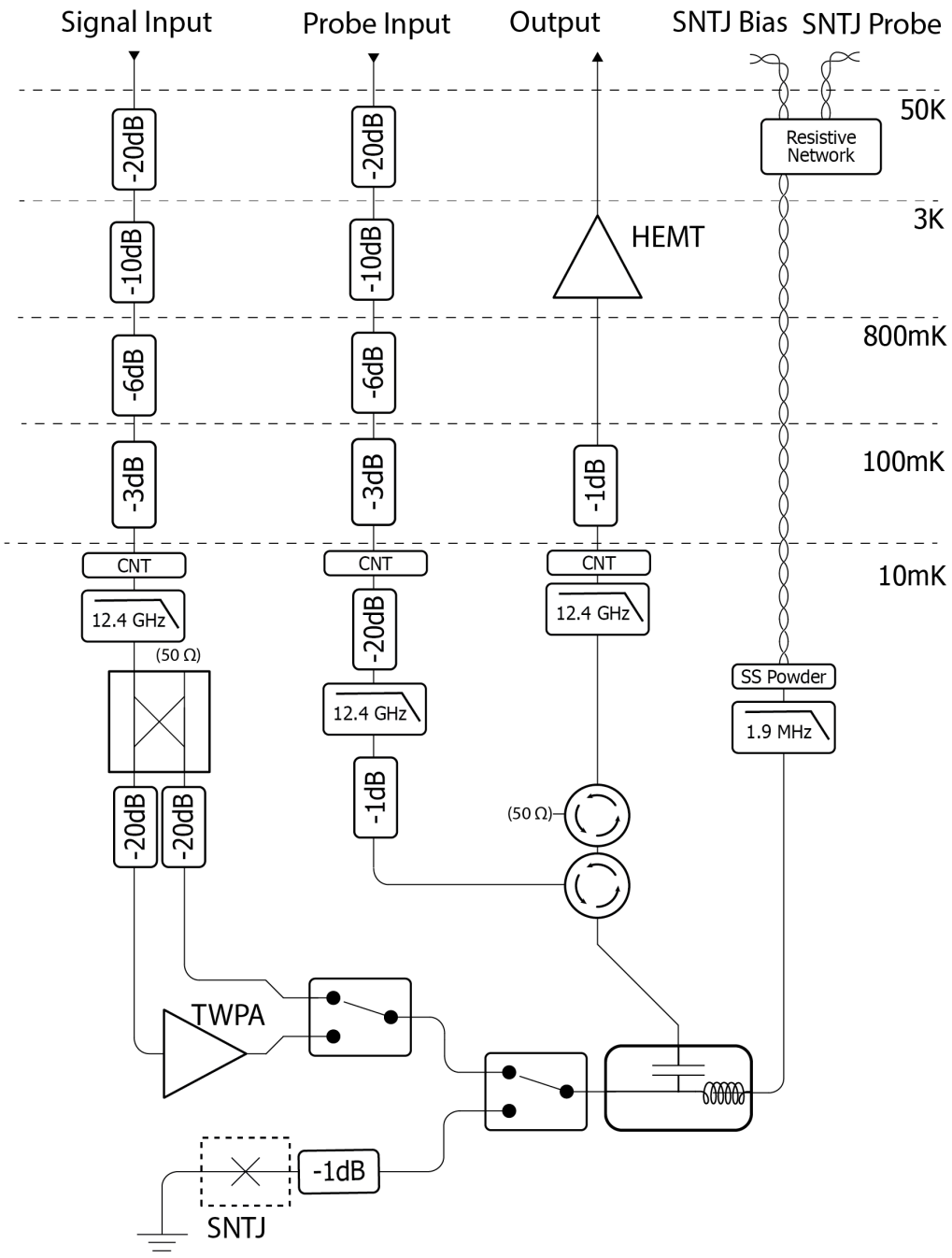

Figure 3.4: Schematic of microwave network inside the dilution refrigerator used to measure the noise temperature and gain of the TWPA. The 3-dB coupler before the TWPA allows for alternating measurement of a through-line and the TWPA. Outside of the dilution fridge, a 3-dB coupler at the signal input combines the pump tone for the TWPA and the probe tone used in the measurement.

3.5 Noise Temperature Measurements of a Travelling Wave Parametric Amplifier

Prior to the main experiment of this thesis characterizing propagating nonclassical states a separate experiment was conducted measuring the noise temperature and gain of the TWPA which would later play a critical role in obtaining the primary results discussed later. While these measurements on the TWPA were not directly necessary to the proceeding experiments, it gave confidence in the device and was served as the first noise temperature measurement made on this commercial TWPA by QuantWare.

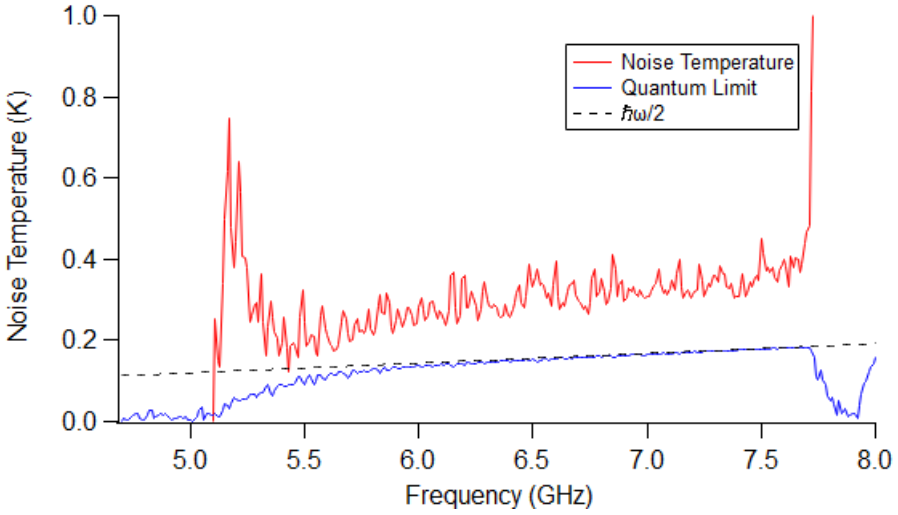

Figure 3.5: Measured noise temperature of the TWPA plotted along with its quantum noise limit which is set by the gain shown in figure (3.1). $\hbar\omega/2$ gives what the quantum limit would be in the case of $G \to \infty$.

As is shown in Figure 3.4, the gain of the TWPA was directly measured by placing it in parallel with a through-line and using a microwave switch to measure the outputed signal and noise strength though each line to obtain a signal-to-noise ratio (SNR) improvement, ΔSNR. To measure the noise temperature, a third channel was used along with its own switch to instead measure the output of the SNTJ through the amplification chain allowing for the TWPA noise and the measurement noise to be distinguished. Fitting with the SNTJ gives the input noise temperature of the amplification chain while the physical temperature obtained from the SNTJ can be used along with the assumption that the input to the TWPA is purely thermal to obtain the noise temperature of the input to the TWPA. This was found to be 63 mK. The

definition of ΔSNR can be expanded in terms of gains and noise powers referred to inputs as follows where the properties of the Josephson TWPA are denoted by subscript, J, and the properties of the proceeding low-noise chain of transistor amplifiers is denoted by subscript LNA:

$$\begin{aligned}\Delta\text{SNR} &= \frac{S_{\text{J,LNA}}}{N_{\text{J,LNA}}}\frac{N_{\text{LNA}}}{S_{\text{LNA}}} = \frac{[G_{\text{LNA}}G_{\text{J}}S_{\text{in}}][G_{\text{LNA}}(N_{\text{LNA}}+N_{\text{in}})]}{[G_{\text{LNA}}(N_{\text{LNA}}+G_{\text{J}}(N_{\text{J}}+N_{\text{in}}))][G_{\text{LNA}}S_{\text{in}}]} \\ &= \frac{G_{\text{J}}(N_{\text{LNA}}+N_{\text{in}})}{N_{\text{LNA}}+G_{\text{J}}(N_{\text{J}}+N_{\text{in}})}.\end{aligned} \tag{3.9}$$

Since we can measure ΔSNR and G_{J} using the TWPA & through-line pair, N_{LNA} with the SNTJ fitting, and can assume N_{in} to be that of a quantum vacuum state from the system's physical temperature, we can easily rearrange (3.9) for N_{J}:

$$N_{\text{J}} = N_{\text{LNA}}\left(\frac{1}{\Delta\text{SNR}}-\frac{1}{G_{\text{J}}}\right)+N_{\text{in}}\left(\frac{1}{\Delta\text{SNR}}-1\right).$$

Finally, since the bandwidth and frequency of all these measurements can be made to be identical, we can use (3.1) to convert the above into an expression of noise photon count or equivalently, noise temperature [30]:

$$T_{N,\text{J}} = T_{N,\text{LNA}}\left(\frac{1}{\Delta\text{SNR}}-\frac{1}{G_{\text{J}}}\right)+T_{N,\text{in}}\left(\frac{1}{\Delta\text{SNR}}-1\right). \tag{3.10}$$

Using the superheterodyne setup described in chapter 3.4, this noise temperature measurement was performed over a wide range of frequencies in the lower passband of the QuantWare TWPA below its dispersive feature. The gain measurements shown in Figure 3.1 demonstrate over 20 dB of gain over a few GHz close to the dispersive feature while the noise temperature measurements shown in Figure 3.5 demonstrate near quantum-limited performance with around 1 photon of added noise from 5.5 GHz to the dispersive feature below around 7.8 GHz.

Chapter 4

Measurement and Entanglement Theory

To measure genuine tripartite entanglement from 3-photon SPDC, we need to be able to obtain moments of field operators of the propagating states emitted from the parametric cavity. However, what we measure at the digitizer is the output of a propagating state that has been amplified and combined with noise modes. Thus, we need to use our knowledge of the amplification chain obtained from SNTJ calibrations as well as chopped measurements to measure the moments of the noise modes combined with the signal and then use this to reconstruct the state emitted from our cavity as is described in chapters 4.1 and 4.2.

In fact to be more rigorous with our description, what we are really measuring is the integrated field over a continuum of modes in the transmission line. In chapter 4.3 we provide a quantum description of exactly what is measured at the digitizer and discuss qualitatively how this maps effectively onto what we wish to learn.

Finally, a discussion of the non-Gaussian behaviour expected from our states is presented in chapter 4.4 and we elucidate how these moments of field operators we obtain can be used to verify the genuine tripartite entanglement produced by 3-photon SPDC in chapter 4.5.

4.1 Quantum Description of Measured Fields

In order to obtain expectation values of operators of our propagating state leaving the cavity, we must write down a quantum mechanical description of our measurement apparatus that we can then invert to find the desired expectations given the classical values that we measure at room temperature. The act of amplifying a propagating state and then measuring both signal quadratures with an ADC can be viewed as applying a Bogoliubov amplification transformation [38] followed by double optical homodyne detection where we split the signal again to measure one quadrature of each output [39].

Amplification of the signal input, $\hat{a}$, using a parametric amp with gain, G', and noise mode, $\hat{h}_{\text{amp}}$, is given by the phase-insensitive transform:

$$\hat{a}_2 = \sqrt{G'}\hat{a} + \sqrt{G'-1}\hat{h}^\dagger_{\text{amp}}.$$

And subsequent double-homodyne detection done at the ADC is given by a beam-splitter transformation with the added noise mode, $\hat{h}_{\text{mix}}$:

$$\hat{a}_3 = \frac{\hat{a}_2 + \hat{h}^\dagger_{\text{mix}}}{\sqrt{2}}$$
$$\hat{a}_4 = \frac{\hat{a}_2 - \hat{h}^\dagger_{\text{mix}}}{\sqrt{2}}.$$

followed by a measurement of the real and imaginary components of $\hat{a}_3$ and $\hat{a}_4$ respectively:

$$\hat{X} = \hat{a}_3 + \hat{a}_3^\dagger$$
$$\hat{P} = -i(\hat{a}_4 - \hat{a}_4^\dagger). \tag{4.1}$$

These quadratures that we measure at the output are equivalent to the components of the complex envelope for our signal input state along with a combined noise mode, $\hat{h}$:

$$\hat{S} = \sqrt{G'/2}(\hat{a} + \hat{h}^\dagger)$$
$$= \frac{\hat{X} + i\hat{P}}{2}.$$

Here, we have combined $\hat{h}_{\text{amp}}$ and $\hat{h}_{\text{mix}}$ into an overall noise mode $\hat{h}$ given by:

$$\hat{h} \equiv \sqrt{\frac{G'-1}{G'}}\hat{h}_{\text{amp}} - \frac{1}{\sqrt{G'}}\hat{h}_{\text{mix}} \tag{4.2}$$

Though in the limit of $G' \gg 1$, $\hat{h} \to \hat{h}_{\text{amp}}$ which is how we will refer to it going forward [40, 7, 39]. Since we empirically measure gain using the SNTJ which includes losses from the cables and power splitters used, we can collect the $\sqrt{2}$ due to the homodyne beam splitter into G' and call this G:

$$\hat{S} \equiv \sqrt{G}(\hat{a} + \hat{h}^\dagger) = \frac{\hat{X} + i\hat{P}}{2}. \tag{4.3}$$

In addition to the fact that the amplitude of $\hat{S}$ is macroscopically large and can be measured with room temperature electronics, it also satisfies $[\hat{S}, \hat{S}^\dagger] = 0$. This is necessary for us to measure both quadratures of $\hat{S}$ exactly and allows us to treat $\hat{S}$ as an effectively classical complex variable.

Later in chapters 4.2 and 4.5, we will be interested in powers of these field operators and our expressions will become quite long. Thus, we will drop the $\sqrt{G}$ in (4.3) from our expressions but recognize that to relate some nth power of $\hat{a}$ or $\hat{h}^\dagger$ to $\hat{S}$, we must multiply by the $G^{\frac{n}{2}}$ corresponding to that mode.

4.2 Converting Measurements to State Expectations

When we measure the field of the output mode, we obtain many samples of $\hat{S}$ over time which could in general allow us to obtain time-correlation functions of $\hat{S}$. In our case, the propagating states we wish to measure are generated by a continuous processes and we are not interested in correlations over time. Thus, we will restrict our attention here to simply the moments of $\hat{S}$. We start by writing down expressions for moments of $\hat{S}$ when the cavity is emitting our state of interest, $\hat{S}_\rho$, and when the cavity is emitting a nearly vacuum state, $\hat{S}_{|0\rangle\langle 0|}$, each as a function of $\hat{a}$ and $\hat{h}$. We then invert our equations for $\hat{S}_\rho$ and $\hat{S}_{|0\rangle\langle 0|}$ to find explicit expressions for the moments of $\hat{a}$.

In general, we wish to characterize states that are inseparable across multiple frequencies. Here we present an outline of how this can be done for just the operators $\langle \hat{a} \rangle$ and $\langle \hat{a}^\dagger \hat{a} \rangle$ to demonstrate methodology.

In the case of $\langle \hat{a} \rangle$, we can write it as

$$\langle \hat{S} \rangle = \langle \hat{a} \rangle + \langle \hat{h}^\dagger \rangle.$$

In the ideal case, the noise mode, $\hat{h}$, would be populated by a vacuum state, whereas in a realistic case it is populated by a thermal state of some temperature given by the

amplification chain's noise temperature. However, in both of these cases, it satisfies $\langle \hat{h}^\dagger \rangle = 0$ and this moment for a state ρ becomes

$$\langle \hat{a} \rangle = \langle \hat{S} \rangle_\rho. \tag{4.4}$$

As another example, we can find $\langle \hat{a}^\dagger \hat{a} \rangle$ with

$$\begin{aligned} \langle \hat{S}^\dagger \hat{S} \rangle &= \langle \hat{a}^\dagger \hat{a} \rangle + \langle \hat{a} \hat{h}^\dagger \rangle + \langle \hat{a}^\dagger \hat{h} \rangle + \langle \hat{h} \hat{h}^\dagger \rangle \\ &= \langle \hat{a}^\dagger \hat{a} \rangle + \langle \hat{h} \hat{h}^\dagger \rangle. \end{aligned}$$

In order to obtain $\langle \hat{a}^\dagger \hat{a} \rangle$ from $\langle \hat{S}^\dagger \hat{S} \rangle$, we need to be able to measure $\langle \hat{h} \hat{h}^\dagger \rangle$ which we expect to be quite large for the thermal state from our amplification chain. This can be done by turning off the parametric pump for the cavity such that the propagating state is reduced to a vacuum state. In reality, the vacuum state is always actually a thermal state with some temperature we typically find to be around $T \approx 70$ mK, but as long as it satisfies $T \ll hf/k_B$−as is the typical assumption for the cavity−it can be well approximated by a vacuum state. Since $\langle \hat{a}^\dagger \hat{a} \rangle$ is 0 for a vacuum state, when we measure $\langle \hat{S}^\dagger \hat{S} \rangle$ with the parametric pump off, we get: $\langle \hat{S}^\dagger \hat{S} \rangle_{|0\rangle\langle 0|} = \langle \hat{h} \hat{h}^\dagger \rangle$ and we can obtain $\langle \hat{a}^\dagger \hat{a} \rangle$ for state ρ with

$$\langle \hat{a}^\dagger \hat{a} \rangle = \langle \hat{S}^\dagger \hat{S} \rangle_\rho - \langle \hat{S}^\dagger \hat{S} \rangle_{|0\rangle\langle 0|}. \tag{4.5}$$

This approach can be generalised to expectations of $\langle (\hat{a}^\dagger)^j (\hat{a})^k \rangle$ for any $j,\ k$ which gives us all normally ordered operator expectations of the propagating state and thus a full description of its statistics. This relies on the fact that all normally ordered operators have $\langle (\hat{a}^\dagger)^j (\hat{a})^k \rangle = 0$ for a vacuum state and thus $\langle (\hat{S}^\dagger)^j (\hat{S})^k \rangle_{|0\rangle\langle 0|} = \langle (\hat{h}^\dagger)^j (\hat{h})^k \rangle$ for any $j,\ k$. As we extend this to higher degrees of j and k, we will obtain dependency on lower degrees of $\langle (\hat{a}^\dagger)^j (\hat{a})^k \rangle$ and so our approach to computing all moments is recursive.

The correlators between propagating fields of different frequencies can be measured using the exact same procedure since $[\hat{S}_a, \hat{S}_b] = 0$. Furthermore, $[\hat{a}, \hat{b}] = [\hat{h}_a, \hat{h}_b] = 0$ which simplifies the subtractions. In general, this can be done for any degree of $\langle (\hat{a}^\dagger)^j (\hat{a})^k (\hat{b}^\dagger)^l (\hat{b})^m (\hat{c}^\dagger)^n (\hat{c})^o \rangle$. Detailed computations of each moment expectation used in the presented results are included in appendix A.

4.3 Continuum operators to single mode operators

4.3.1 Continuum Measurements from the Digitizer

So far in this thesis, we have entirely written states of the electromagnetic field as singular annihilation and creation operators, $\hat{a}$ and $\hat{a}^\dagger$. This treatment is correct in the limit of a perfectly enclosed and lossless optical cavity, but we are interested in describing the states in a propagating field through a continuum which in general must be written as a sort of densities of modes $\hat{a}(\omega)$, $\hat{S}(\omega)$ satisfying $[\hat{a}(\omega), \hat{a}^\dagger(\omega')] = \delta(\omega - \omega')$, $[\hat{S}(\omega), \hat{S}^\dagger(\omega')] = 0$. We can then relate these continuum operators in frequency space to operators in time defined using the Fourier transform:

$$\hat{a}(t) = \sqrt{\frac{1}{2\pi}} \int_{-\infty}^{\infty} \mathrm{d}\omega \hat{a}(\omega) e^{-i\omega t} \tag{4.6}$$

$$\hat{S}(t) = \sqrt{G} \int_{-\infty}^{\infty} \sqrt{\frac{1}{2\pi}} \mathrm{d}\omega \left[\hat{a}(\omega) e^{-i\omega t} + \hat{h}^\dagger(\omega) e^{i\omega t} \right]. \tag{4.7}$$

These continuum operators similarly give us a direct description of the observable that we actually measure using the ADCs which is a voltage over time [41]

$$\hat{V}(t) = \sqrt{\frac{\hbar Z_0}{4\pi}} \int_{\omega_0 - \pi B}^{\omega_0 + \pi B} \mathrm{d}\omega \sqrt{\omega} \left[\hat{S}(\omega) e^{-i\omega t} + \hat{S}^\dagger(\omega) e^{i\omega t} \right] \tag{4.8}$$

$$= \sqrt{\frac{\hbar Z_0}{4\pi}} \int_{\omega_0 - \pi B}^{\omega_0 + \pi B} \mathrm{d}\omega \sqrt{\omega} \left[\hat{X}(\omega) \cos(\omega t) + \hat{P}(\omega) \sin(\omega t) \right] \tag{4.9}$$

where the frequency integrals are performed only over the bandwidth of our measurement instrument, B.

The fact that we can actually write the the signal as a function of time may seem to present an issue to measuring expectation values which require us to make repeated independent and identically distributed (iid) measurements of the signal. This issue is resolved by the fact that the signal is produced from photons generated in the cavity and then leaking out over the cavity's photon lifetime and so measurements separated by more than this lifetime should be iid.

4.3.2 Conversion into Discrete Modes

However, for our calculations we are only interested in the phase-space statistics of the propagating states. This means that we can instead consider discrete operators $\hat{a}_f,\ \hat{S}_f$ corresponding to a temporal mode-profile $f(t)$ over an interval which we expect to contain all of the relevant statistics. Following Loudon [42], we define

$$\hat{a}_f = \int_0^\infty \mathrm{d}t\ \hat{a}(t) f(t) \tag{4.10}$$

$$\hat{S}_f = \int_0^\infty \mathrm{d}t\ \hat{S}(t) f(t) \tag{4.11}$$

where $f(t)$ obeys $\int_0^\infty \mathrm{d}t |f(t)|^2 = 1$ and in the case of our measurement scheme, it can be made to correspond to the integration window of the detectors used to obtain a single sample. In order to say that each separate sample is an independent measurement of a single temporal mode, we again must satisfy the requirement that the time between periods exceeds any expected correlations. Making this transformation comes at the cost of losing information on the spectral/temporal details of the signal. However, our new mode operators once again behave as discrete mode operators of the electromagnetic field and so satisfy $[\hat{a}_f, \hat{a}_f^\dagger] = 1,\ [\hat{S}_f, \hat{S}_f^\dagger] = 0$ and all of the previously derived methodology from sections (4.2, 4.1) again hold. Since we are only interested in one temporal mode for each cavity frequency, we will drop the subscript f from here on out [43, 39].

4.3.3 Digitizer Output to Moments

To think about the exact signal measured at the ADC, we recognize that the bandwidth of the apparatus is set to be 1 MHz which is about 10^3 times smaller than the cavity frequencies. Since the signal measured is narrow band, we can think of the voltage and its quadratures as a phasor and define a complex voltage. This makes the connections between $\hat{V}(t)$ and $\hat{S}(t)$ much clearer and aligns our analysis more closely with the moments we wish to measure. Moreover, this measurement is made after a series of analog and digital mixing steps resulting in the signal taking the form of a fluctuating baseband signal, where we use the fact that our measurement is over a

narrow band and so we can treat $\sqrt{\omega}$ as constant at the cavity frequency, ω_0:

$$\begin{aligned}\tilde{V}(t) &= \frac{\hat{I}_{\text{Base}}(t) + i\hat{Q}_{\text{Base}}(t)}{\sqrt{2}} \\ &= \sqrt{\frac{\hbar\omega_0 Z_0}{2}}\left[\frac{\hat{X}_{\text{Base}}(t) + i\hat{P}_{\text{Base}}(t)}{\sqrt{2}}\right] \\ &= \sqrt{\hbar\omega_0 Z_0}\hat{S}_{\text{Base}}(t). \end{aligned} \tag{4.12}$$

We can then set the mode profile, $f(t)$, to be a window of length τ and height $1/\sqrt{\tau}$ which also defines our bandwidth such that $B = 1/\tau$. We can then directly connect the discrete operator we would like to measure to the sampled voltage phasors recorded by the ADC, $\tilde{V}_{\text{ADC}}$:

$$\begin{aligned}\hat{S} &\equiv \int_0^\tau \mathrm{d}t \frac{1}{\sqrt{\tau}}\hat{S}_{\text{Base}}(t) \\ \tilde{V}_{\text{ADC}} &\equiv \frac{1}{\tau}\int_0^\tau \mathrm{d}t\tilde{V}(t) \\ \hat{S} &= \sqrt{\frac{1}{\hbar\omega_0 B Z_0}}\tilde{V}_{\text{ADC}}. \end{aligned} \tag{4.13}$$

Thus when we measure the moments of $\hat{S}$, we are actually measuring the complex voltage, $\tilde{V}$, collected over the temporal mode that is reported by the digitizer. We then taken some power of this to obtain a moment. Dropping the subscript ADC, this can be expanded as

$$\begin{aligned}&\left\langle \hat{S}^n[\hat{S}^\dagger]^m \right\rangle \\ &= \left(\frac{1}{\hbar\omega_0 B Z_0}\right)^{\frac{n+m}{2}} \left\langle \tilde{V}^n[\tilde{V}^\dagger]^m \right\rangle \\ &= \left(\frac{B}{\hbar\omega_0 Z_0}\right)^{\frac{n+m}{2}} \left\langle \left[\int_0^\tau \mathrm{d}t\tilde{V}(t)\right]^n \left[\int_0^\tau \mathrm{d}t\tilde{V}^\dagger(t)\right]^m \right\rangle \\ &= \left(\frac{B}{\hbar\omega_0 Z_0}\right)^{\frac{n+m}{2}} \left\langle \int_0^\tau \mathrm{d}t_1 \ldots \int_0^\tau \mathrm{d}t_{n+m} \left[\tilde{V}(t_1)\ldots\tilde{V}(t_n)\tilde{V}^\dagger(t_{n+1})\ldots\tilde{V}^\dagger(t_{n+m})\right] \right\rangle. \end{aligned} \tag{4.14}$$

We can recognize then that the $(n,m)_{\text{th}}$ moment reported is actually the $(n,m)_{\text{th}}$-order autocorrelation function averaged over the defined temporal mode. It is this integration over the temporal mode that leads to the loss of information about the time correlations of our signal. We can think of the choice of $f(t)$ as a sort of mode matching to the temporal mode in which our signal of interest exists. Though obviously we should not expect a square window to be the optimal mode profile. However, if some moment of $\hat{S}$ and $\hat{S}^\dagger$ is measured over a poorly matched window such that some integrated signals have no correlation, this only appears as a loss of measurement efficiency of the signal and does not affect our measured statistics.

4.4 Non-Gaussian Multimode Entangled States

A transmission line cavity terminated by a symmetric DC-SQUID was shown in chapter 2.6 to be capable of producing quadratic interaction Hamiltonians between modes of the cavity. These quadratic parametric interactions can be produced using a wide variety of physical systems and yield a very well studied set of transformations. It can be shown that quadratic and linear Hamiltonians will only ever generate transformations that are Gaussian, meaning they map the set of all Gaussian states onto itself [44]. The set of Gaussian states exhibits measurement statistics entirely governed by Gaussian distributions and thus can be entirely described by only the 1st and 2nd moments.

Since most spontaneous parametric interaction experiments are done by evolving a vacuum state − which is Gaussian − under a quadratic Hamiltonian, the resulting state is always Gaussian. Multimode entangled Gaussian states have been generated using this general scheme [45, 46] and their entanglement can be measured using a variety of entanglement tests dependent on the variances and covariances between quadratures of the entangled modes [47, 48].

These Gaussian operations and Gaussian multimode entangled states themselves can be valuable resources for example in quantum networks [49] though they lack the ability to perform universal quantum computation if they are only paired with linear measurements. Conversely, non-Gaussian entangled states have been found to posses advantages over Gaussian states in tasks like quantum metrology [50]. In the case of quantum computation, it has been shown that continuous-variable circuits consisting of Gaussian input states and Gaussian operations which have access to ancillary modes populated by specific non-Gaussian states known as cubic phase states are sufficient for universal quantum computation [38]. Critically, the interactions that we can produce with our asymmetric SQUID-terminated parametric cavity have

cubic Hamiltonians which means that they are expected to generate non-Gaussian transformations and subsequently non-Gaussian propagating states.

Unfortunately since these states are non-Gaussian, we also cannot expect potential entanglement to be captured by sufficient conditions based on their 1st and 2nd moments. Indeed, it has been shown that the states theoretically generated by a three mode Trisqueezing Hamiltonian shown in equation (2.36) entirely fail to demonstrate entanglement using sufficient but not necessary conditions based on covariance matrices between modes [51]. Instead, entirely different conditions must be used to observe tripartite entanglement based on higher moments of the states.

4.5 Non-Gaussian Tripartite Entanglement

One class of sufficient entanglement conditions that has proven particularly useful for observing entanglement in non-Gaussian states are Hillery-Zubairy conditions. These conditions are based on the fact that any pair of operators $\hat{A}^{(1)}, \hat{A}^{(2)}$ acting on subspaces (1) and (2) of a partitioned Hilbert space must satisfy [52]

$$\left|\left\langle \hat{A}^{(1)}\hat{A}^{(2)}\right\rangle\right| \leq \sqrt{\left\langle \hat{A}^{(1)\dagger}\hat{A}^{(1)}\right\rangle \left\langle \hat{A}^{(2)\dagger}\hat{A}^{(2)}\right\rangle} \tag{4.15}$$

and any state which violates this inequality must be inseparable with respect to the partition into subspaces (1) and (2). We will denote our modes a, b, and c with annihilation operators $\hat{a}, \hat{b}, \hat{c}$ and consider the each of the bipartitions of the Hilbert space into a single and a pair of frequency modes:

$$\rho_1 = \rho_a \otimes \rho_{bc}, \quad \rho_2 = \rho_b \otimes \rho_{ac}, \quad \rho_3 = \rho_c \otimes \rho_{ab}. \tag{4.16}$$

It has been shown that a choice of operators which should rule out each of the bipartitions is given by the annihilation operator on the single mode and a pair of them on the other two [53]. For example, to place a condition on the bipartitioned state ρ_1, our operators are $\hat{A}^{(1)} = \hat{a}$ and $\hat{A}^{(2)} = \hat{b}\hat{c}$ and we obtain

$$|\langle \hat{a}\hat{b}\hat{c}\rangle| \leq \sqrt{\left\langle \hat{N}_a\right\rangle \left\langle \hat{N}_b\hat{N}_c\right\rangle}. \tag{4.17}$$

where $\hat{N}_a, \hat{N}_b, \hat{N}_c$ are the number operators on modes a, b, and c respectively. If our state violates (4.17) for all permutations over all pairings of a, b, and c then we can rule out all bipartitions and it is defined to be fully inseparable. However, to say

that the state is genuinely entangled we need to rule out the possibility that it is a probabilistic mixture of biseparable states:

$$\rho = P_1\rho_1 + P_2\rho_2 + P_3\rho_3. \tag{4.18}$$

If we measure the expectation of $\hat{a}\hat{b}\hat{c}$ for ρ, $\langle\hat{a}\hat{b}\hat{c}\rangle_\rho$, and for each of its constituent states ρ_1, ρ_2, and ρ_3, then we can write a triangle inequality on $|\langle\hat{a}\hat{b}\hat{c}\rangle|$ using equation 4.18 to obtain

$$|\langle\hat{a}\hat{b}\hat{c}\rangle|_\rho \leq P_1|\langle\hat{a}\hat{b}\hat{c}\rangle|_{\rho_1} + P_2|\langle\hat{a}\hat{b}\hat{c}\rangle|_{\rho_2} + P_3|\langle\hat{a}\hat{b}\hat{c}\rangle|_{\rho_3}. \tag{4.19}$$

Next we can substitute our inequality (4.17) for each of ρ_1, ρ_2, ρ_3 in to (4.19):

$$|\langle\hat{a}\hat{b}\hat{c}\rangle|_\rho \leq P_1\sqrt{\left\langle\hat{N}_a\right\rangle\left\langle\hat{N}_b\hat{N}_c\right\rangle} + P_2\sqrt{\left\langle\hat{N}_b\right\rangle\left\langle\hat{N}_a\hat{N}_c\right\rangle} + P_3\sqrt{\left\langle\hat{N}_c\right\rangle\left\langle\hat{N}_a\hat{N}_b\right\rangle} \tag{4.20}$$

We would like to find some expression of operators like (4.17) that is true for any state of the form of (4.16). We can use the fact that this is a convex sum over these expectation expressions $\sqrt{\langle N_i\rangle\langle N_jN_k\rangle}$ since probabilities must sum to 1. This means that the maximum value that the RHS of (4.20) can take over all ρ is simply where P_i is 1 for whichever of ρ_i has the largest $\sqrt{\langle N_i\rangle\langle N_jN_k\rangle}$. This yields:

$$|\langle\hat{a}\hat{b}\hat{c}\rangle| \leq \max_{\substack{i,j,k=a,b,c\\ i\neq j\neq k\neq i}} \sqrt{\left\langle\hat{N}_i\right\rangle\left\langle\hat{N}_j\hat{N}_k\right\rangle} \tag{4.21}$$

Any state violating (4.21) cannot be described by any state of the form (4.16) and thus possesses genuine tripartite entanglement[53].

Finally, we can rearrange this expression to obtain a single value that we can compute to assess the entanglement of our state:

$$G = |\langle\hat{a}\hat{b}\hat{c}\rangle| - \max_{\substack{i,j,k=a,b,c\\ i\neq j\neq k\neq i}} \sqrt{\left\langle\hat{N}_i\right\rangle\left\langle\hat{N}_j\hat{N}_k\right\rangle} \leq 0 \tag{4.22}$$

We now have a very simple form of our entanglement condition: positivity of G and thus violation of (4.22) for a given state is a sufficient but not necessary condition for possessing non-Gaussian genuine tripartite entanglement.

Chapter 5

Results

5.1 Device and Measurement Tune-Up

After fabricating the device depicted in figure 2.4, it was packaged and installed inside of the dilution fridge along with the QuantWare TWPA and the NIST SNTJ according to the schematic given in figure 3.2. With the mixing chamber of the dilution fridge cooled to less than 10 mK, a parametric pump for the TWPA was sent down the TWPA Pump line to activate its amplification. Tones were sent down the Input line using a Vector Network Analyzer (VNA) first to find the approximate frequency of each cavity mode as they are highly sensitive to inconsistent junction parameters. Next, tones from the VNA were again scattered off the cavity while the DC flux applied with the coil was varied. This allowed for the determination of the existing background flux offset using the fact that the external flux through the SQUID changes its impedance and consequently the cavity frequency. As can be seen in equation (2.32), an external flux bias close to 0 gives the largest cubic terms in the Hamiltonian and so the DC flux bias was set accordingly.

Next, the SNTJ was used to obtain the noise temperatures of the amplification chain at the frequency of each cavity mode. The power and frequency of the TWPA pump drive were then swept to minimize the noise temperature at each mode. The loose heuristic used to combine each noise temperature into one was to take the maximum of all three temperatures at each mode and adjust the pump to minimize it. The minimized noise temperatures of the amplification chain is reported in table 5.1.

Finally, a parametric pump drive was sent into the cavity at the sum of three cavity mode frequencies and its emitted radiation was measured according to the scheme

f (GHz)	Gain $\times 10^6$	$T_N(K)$
5.560	11.69	1.05
6.831	15.35	0.62
7.902	72.37	0.32

Table 5.1: Gain and Noise Temperature at each mode measured by the SNTJ. The three frequencies at which the amplification chain is do not exactly match the frequencies of the cavity modes under a parametric drive since they will shift for every pump power. This systematic error is negligible as the calibration frequency differs from the driven cavity frequencies by less than 1 MHz over which the gain and noise temperature is effectively constant.

described in chapter 3. The power and frequency of this pump (herein just called the parametric pump) was also swept, this time to maximize the coskewness of the signals at each of the three frequencies which is expected to be highly nonzero for these non-Gaussian states and yet must always be 0 for Gaussian noise produced by the amplifiers. Sweeps over all power and frequencies are necessary as the parametric drive induces an effective Kerr-shift on the cavity frequencies as its power is increased and parametric pump frequency must be adjusted accordingly. Furthermore, higher-order nonlinearities, cavity heating, and oscillations due to photon production overpowering the loss-rate can all lead to unwanted and incoherent effects as the parametric pump power is is varied. Therefore, power spectral densities and the field quadrature histograms measured at the digitizer are qualitatively examined to select a parametric pump power and frequency that is producing the desired multimode trisqueezed states from 3-photon spontaneous parametric down-conversion. The use of qualitative tests is not problematic since states produced from poorly chosen pumping condition will simply not violate our entanglement condition at which point we can reassess our choice of condition.

5.2 Violation of Non-Gaussian Entanglement Witness

After tuning up the device using the steps described in chapter 5.1, we can now measure the operator expectations necessary to violate our entanglement condition. To be able to compute the operator expectations desired, we first use the SNTJ to obtain the gain of the amplification chain, then perform chopped measurements of the

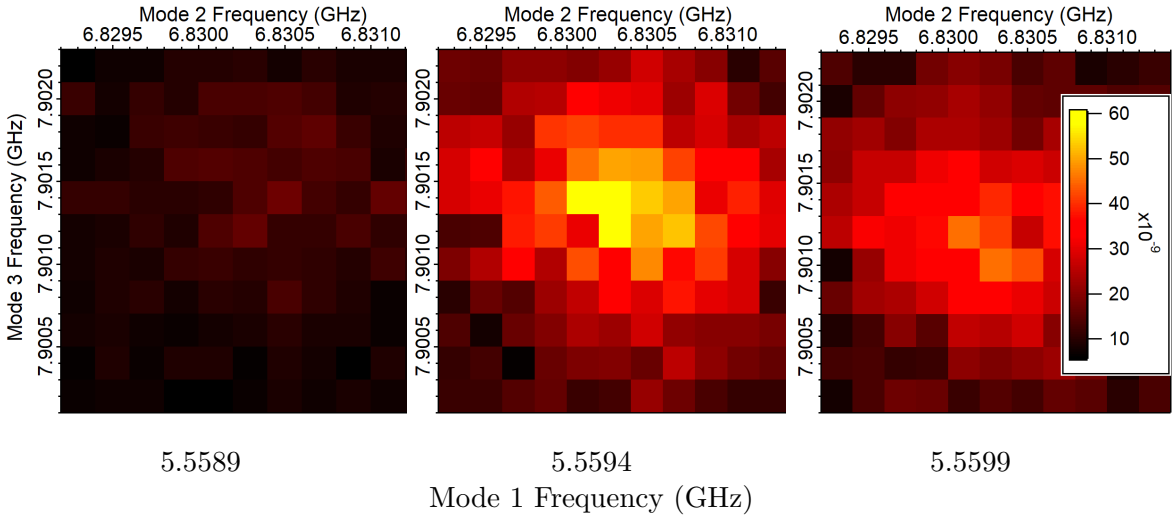

Figure 5.1: A 3D sweep of total coskewness over measurement frequency of all three digitizers while pumping at 14dBm. The parametric pump is always set to the sum of the three measurement frequencies. Total coskewness is loosely defined as the sum of squares of all eight coskew combinations between the two quadratures of each mode. This loose measure of tripartite correlations is used to observe what parametric drive conditions produce strong 3-photon SPDC and at what exact frequencies are the photons produced

outputted signal from the cavity where we use a microwave switch to drive with the parametric pump for the ON measurements and switch the Pump Input line to a 300 K 50 Ω load for the OFF measurements. After obtaining moments of the outputted signal with the parametric ON and OFF, the subtractions described in chapter 4.2 can be performed finally resulting in the operators used in equation (4.22).

The optimal power and frequency selected for the parametric pump was 15 dBm and 20.2915 GHz respectively corresponding to output signals measured at three frequencies given in table 5.2. Under these conditions the value for the witness was measured to be $G = 0.054 \pm 0.003$. This violates the entanglement witness by 15 sigmas providing a convincing demonstration of the non-Gaussian genuine tripartite entanglement of propagating states from 3-photon spontaneous parametric down-conversion.

Additionally, we can fix the pump power at several values around and below the optimum value and then optimize the pump frequency at each power. Despite the complex behaviour of the cavity under strong driving, the power of the parametric pump should map monotonically onto the strength of the parametric interaction,

Mode	f (GHz)
a	5.5596
b	6.8304
c	7.9015
Pump	20.2915

Table 5.2: Tuned frequencies of pump drive and each measurement digitizer when parametrically pumping at 15 dBm yielding the highest observed entanglement witness value of $G = 0.054 \pm 0.003$.

g_{lmn}, in equation (2.36) and so by measuring G at these different pump powers, we can see how it changes under trisqueezing strength. We observe that the value of G is positive for a pump strength as low as 0 dBm and grows until 15 dBm beyond which it sharply drops off and turns negative. The negativity of G in this regime may signify the destruction of tripartite entanglement. Though since our witness is not a necessary condition for entanglement, it is also possible that the photon correlations have changed such that the entanglement can no longer be detected by our witness. Beyond 16 dBm, we see a significant increase in the output power from the cavity suggesting the onset of some new dynamics beyond the intended cubic Hamiltonian. This leads us to hypothesize that the entanglement is in fact destroyed at these highest parametric pump powers.

5.3 Error Analysis of Tripartite Non-Gaussian Entanglement Witness

Since the entanglement witness, G, uses the expectation of a 4th moment of the annihilation operators, these measured values are dominated by noise from the amplification chain and thus must be averaged over multiple hours for the uncertainty in the subtracted values to be small enough that we can state G with small error. These measurements over long periods of time create a dependency on the long term stability of the measurement and exposes our measurements to fluctuations on a multitude of timescales.

To compartmentalize our discussion, we can treat fluctuations in our apparatus on a timescale within a measurement period and uncertainties that are constant beyond a measurement period separately. These short timescale fluctuations are predominantly

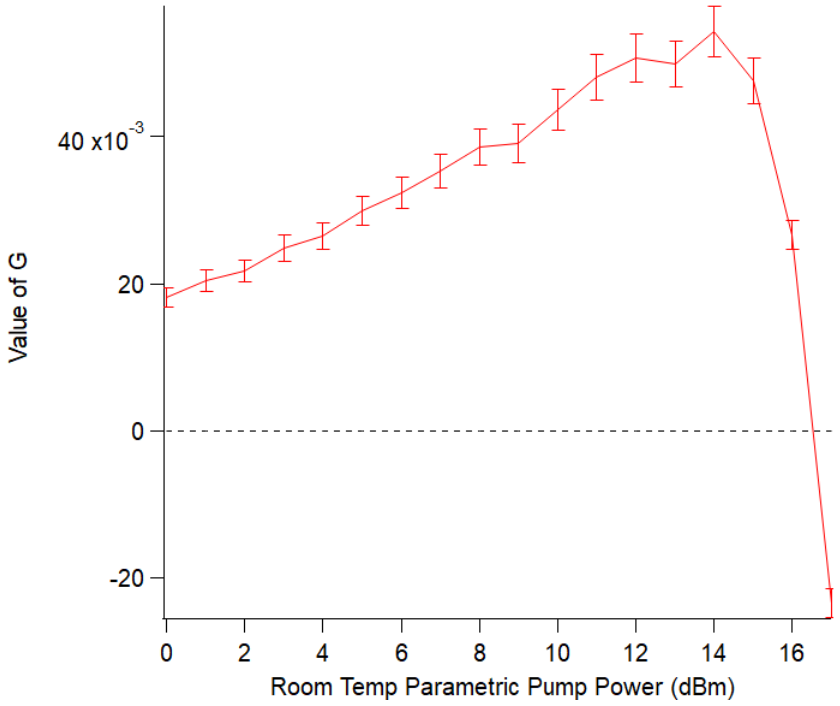

Figure 5.2: The values of G obtained over a range of parametric pump powers. Around a power of 16 dBm we see the output power from the cavity increase significantly suggesting some incoherent dynamics begin to occur and consequently conceal or destroy the entanglement.

due to random error introduced by the Gaussian noise of the amplification chain as well as periodic oscillations in the laboratory infrastructure on the order of several minutes. The long timescale uncertainty is understood to be due to drift in the gain of the amplification chain that occurs between the time it was calibrated with the SNTJ and the time when a given measurement was taken. While this gain drift is fundamentally random it cannot be averaged away since it is due to fluctuations outside the measurement period and with timescales longer than a period. Thus we view it as a systematic error and added it separately to the random error as a sort of global uncertainty.

5.3.1 Systematic Error Due to Drift

The gain used in the conversion from room temperature moments to operator expectations of the cavity output is computed using the SNTJ fitting protocol described

in chapter 3.3. However, there is typically a period of an hour or more in between this calibration and the measurement during which we understand that the gain of the amplification chain will drift. Since this is happening on a longer timescale than our measurement period and largely over a segment of time that we do not measure, we treat it as a systematic error separate from the random errors that will be characterized in chapters 5.3.2 and 5.3.4.

To quantify this uncertainty, we measure the output noise power of the amplification chain with the parametric pump turned OFF over several measurement periods that are identical to those used to compute the entanglement witness. Since from equation (3.2) the noise power is proportional to gain, denoted Gain (since G is the entanglement witness), the relative uncertainty of the noise power over these periods is the same as the relative uncertainty in gain, δGain, assuming the noise temperature is a deterministic variable:

$$\begin{aligned}\frac{\sqrt{\text{Var}(N_{\text{out}})}}{\langle N_{\text{out}}\rangle} &= \frac{\sqrt{\langle (k_B T_n B\ \text{Gain})^2\rangle - \langle k_B T_n B\ \text{Gain}\rangle^2}}{\langle k_B T_n B\ \text{Gain}\rangle} \\ &= \frac{\sqrt{\langle \text{Gain}^2\rangle - \langle \text{Gain}\rangle^2}}{\langle\ \text{Gain}\rangle} \\ &= \frac{\sqrt{\text{Var}(\text{Gain})}}{\langle \text{Gain}\rangle} \equiv \delta\text{Gain}\end{aligned}$$

We then obtain gain variances for each of the three modes and can perform an error propagation on these relative uncertainties. Since each measured field is proportional to $\sqrt{\text{Gain}}$, it is easy to see that for any bipartition:

$$G \propto \sqrt{\text{Gain}_a \text{Gain}_b \text{Gain}_c}$$

And so the relative error in G due to propagated long timescale gain uncertainty is:

$$\delta G = \frac{\delta\text{Gain}_a + \delta\text{Gain}_b + \delta\text{Gain}_c}{2} \tag{5.1}$$

It is not impossible that the noise temperature also fluctuates adding its own contribution to the relative variance of the noise power. However, this can only lead to us overestimating the drift in Gain which means we are at least placing an upper bound on this uncertainty. We find that over time bins equal to our measurement period, the relative uncertainty is: $\delta G = 5.5\%$ which we then convert to an absolute

uncertainty using $\langle G \rangle$ and sum it with the random error found in chapter 5.3.4. Since this uncertainty is defined by our inability to measure it for a given sample set, we will take the conservative assumption that there may be some correlation between drifts of different timescales and thus we will sum the systematic and random errors linearly, rather than under quadrature.

5.3.2 Random Error & Averaging

To quantify the resulting uncertainty from fluctuations within a timescale of a measurement period, we can consider the character of the repeated samples of the outputted signal over a measurement period. The mean of any finite set of independent samples on a constant random variable will always have noise due to the existing variance of the random variable being measured. This can be seen easily from considering a sum of N independent and identically distributed random variables, X_n:

$$\bar{X} = \sum_{n}^{N} \frac{X_n}{N}$$

We wish to consider their variance which will simply add together since each of X_n are independent of each other:

$$\begin{aligned} \mathrm{Var}(\bar{X}) &= \sum_{n}^{N} \frac{\mathrm{Var}(X_n)}{N^2} \\ &= \sum_{n}^{N} \frac{\sigma_x^2}{N^2} \\ &= \frac{\sigma_x^2}{N} \end{aligned} \tag{5.2}$$

While averaging is simple to implement and quantify for identically distributed random variables, fluctuations in the amplifier gain has a strong autocorrelation which means that it will only be averaged out if the sampling timescale is longer than the autocorrelation. Furthermore, these gain fluctuations are correlated over amplification frequencies and so the covariance between different moments measured must be included in any error analysis as is discussed in chapter 5.3.3.

5.3.3 Characterizing Random Error

The ON and OFF measurements are done over alternating 1 second (10^6 data points) measurements collecting subensembles of data. These interleaved measurements ensure that subtracted moments are made using data taken over identical amplification conditions. We can compute each ON and OFF signal moment for each subensemble and then perform the subtractions to obtain the quantum moments of each subensemble. In general, operations performed on moments should always be done after all data is averaged which might seem to suggest this is an issue since we are subtracting moments found from small subensembles of data. However, this is ok since subtraction is linear and commutes with averaging:

$$\sum_{i}^{N} \frac{X_i}{N} - \sum_{j}^{N} \frac{Y_j}{N} = \sum_{k}^{N} \frac{X_k - Y_k}{N} \tag{5.3}$$

The linearity of the operations used to obtain the quantum moments from the room temperature moments also enables us to directly compute variance of the quantum moments rather than computing variance of room temperature variance and propagating error to find quantum variance as will be used later. We now have a set of N measurements of each moment used in the entanglement bound from which we can compute means, variances, and covariances. The means are used to obtain the value of the bound while the variances and covariances computed over subensembles directly give us the uncertainties to be used in error propagation for error in the bound.

By treating the moments computed for each subensemble as a single sample in a time-series of moment measurements, we can directly compute the error correlations between different moments. This is necessary since we understand amplifier drift has a correlated and multiplicative effect on all moments. This binning method allows us to directly observe the variance of our measurements within 1 bin of averaging but we are forced to extrapolate using the standard-error-in-the-mean to obtain a total error after averaging all bins. We can assess the limit of this method by taking exceptionally long measurements and examining the variance between bins as we increase the size of the bin as seen in figure 5.3. Eventually the variance will saturate which indicates the number of samples where the random measurement error is no longer dominant and remaining error is due to long timescale drift which cannot be averaged away. We can then use this as the time limit for our averaging.

One might ask if after finding a time limit, we can set the bin size to 1 sample and compute variances and covariances on every measured data point of the signal. However, this forces us to extend the standard-error-in-the-mean assumption further.

Moreover, our moments actually become ill-defined since the n_{th} moment is only defined for n or more data points. In practice, we select our bin size to match the interleaving period which avoids issues of time between samples or between bins being inconsistent. Alternatively, one may ask if we can simply skip all of the complication of error analysis by computing the entanglement bound directly for each subensemble and then extracting a value and total error in the bound by looking at its mean and variance over subensembles. Unfortunately, this is not equivalent to computing the moments over all subensembles before computing the bound since the calculation for the bound requires multiplication and square root which are both nonlinear operations and do not commute with averaging: $\overline{f(x)} \neq f(\bar{x})$.

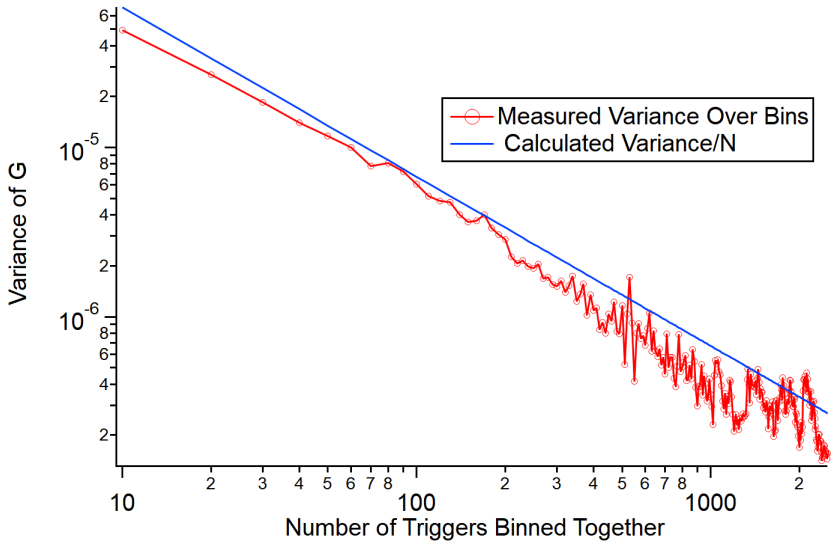

Figure 5.3: A comparison of calculated error in G and empirically measured error. The calculated error is simply found by measuring the variance of each moment over 10,000 triggers, propagating to a variance in G with (5.13) and dividing by N. The empirical error is found from measured variance of G over 10,000/N bins each containing N triggers

5.3.4 Error Propagation of Random Error

Since the moments obtained are from a large number of samples of the signal, we can describe each moment measured as a random variable, X with a mean, $\bar{X}$, and variance, σ_X^2, obeying $\sigma \ll X$.

To perform error propagation, we would like to write down an algebraic expression for the entanglement bound though unfortunately, its computation involves the use of a max() function over all 3 possible bipartitions. To simplify analysis and give a conservative error estimate, we will simply treat each bipartitions separately where we then use the largest uncertainty found for any bipartition as the uncertainty for the overall bound.

To aid in analysis, we will introduce the variable $\tilde{X} \equiv X - \bar{X}$ such that X can be written $X = \tilde{X} + \bar{X}$ where we have now split X into a deterministic component, $\bar{X}$ and a random mean-0 component $\tilde{X}$. Looking at the moments computed over M samples for one example biparition, $\rho = \rho_a \otimes \rho_{bc}$, we will substitute the following variables for readability:

$$X \equiv \left\langle \hat{N}_a \right\rangle_M \tag{5.4}$$

$$Y \equiv \left\langle \hat{N}_b \hat{N}_c \right\rangle_M \tag{5.5}$$

$$Z \equiv \left\langle \hat{a}\hat{b}\hat{c} \right\rangle_M \tag{5.6}$$

The bound for a single bipartition is then:

$$G = Z - \sqrt{X}\sqrt{Y} \tag{5.7}$$

As per the standard technique of error propagation, we can expand $\sqrt{X}$ as a Taylor expansion around $\bar{X}$ under the assumption that $\tilde{X}$ scaled by the derivatives of $\sqrt{X}$ is very small.

$$\sqrt{X} \approx \sqrt{\bar{X}} + \left.\frac{\partial\sqrt{X}}{\partial X}\right|_{X=\bar{X}} \tilde{X} = \sqrt{\bar{X}} + \frac{1}{2\sqrt{\bar{X}}}\tilde{X} \tag{5.8}$$

$$\sqrt{Y} \approx \sqrt{\bar{Y}} + \frac{1}{2\sqrt{\bar{Y}}}\tilde{Y} \tag{5.9}$$

To find an full expression for the variance of G that includes correlations between

X, Y, and Z, we will directly write down and then expand the definition of G:

$$\begin{aligned}
\mathrm{Var}\left(Z - \sqrt{X}\sqrt{Y}\right) &= \left\langle \left(Z - \sqrt{X}\sqrt{Y}\right)^2 \right\rangle - \left\langle Z - \sqrt{X}\sqrt{Y} \right\rangle^2 \\
&= \langle Z^2 \rangle + \left\langle \left(\sqrt{X}\sqrt{Y}\right)^2 \right\rangle - 2\left\langle Z\sqrt{X}\sqrt{Y} \right\rangle \\
&- \left[\langle Z \rangle^2 + \left\langle \sqrt{X}\sqrt{Y} \right\rangle^2 - 2\langle Z \rangle \left\langle \sqrt{X}\sqrt{Y} \right\rangle \right] \\
&= \mathrm{Var}\left(Z\right) + \mathrm{Var}\left(\sqrt{X}\sqrt{Y}\right) - 2\left[\left\langle Z\sqrt{X}\sqrt{Y} \right\rangle - \langle Z \rangle \left\langle \sqrt{X}\sqrt{Y} \right\rangle \right]
\end{aligned} \tag{5.10}$$

We can nicely treat each term in the bottom line separately. We will start with $\mathrm{Var}\left(\sqrt{X}\sqrt{Y}\right)$ where we will first treat $\sqrt{X}$ and $\sqrt{Y}$ as just variables and then substitute in $\overline{\sqrt{X}} = \sqrt{\bar{X}}$ and $\widetilde{\sqrt{X}} = \tilde{X}/\left(2\sqrt{\bar{X}}\right)$. We will also have to make the approximation that $\widetilde{\sqrt{Y}}$ and $\widetilde{\sqrt{X}}$ are small and so we can drop any term with a degree larger than 2 between both of them:

$$\begin{aligned}
&\mathrm{Var}\left(\sqrt{X}\sqrt{Y}\right) \\
&= \left\langle \left(\overline{\sqrt{X}} + \widetilde{\sqrt{X}}\right)^2 \left(\overline{\sqrt{Y}} + \widetilde{\sqrt{Y}}\right)^2 \right\rangle - \left\langle \left(\overline{\sqrt{X}} + \widetilde{\sqrt{X}}\right)\left(\overline{\sqrt{Y}} + \widetilde{\sqrt{Y}}\right) \right\rangle^2 \\
&\approx \overline{\sqrt{X}}^2 \left[\left\langle \widetilde{\sqrt{Y}}^2 \right\rangle - \left\langle \widetilde{\sqrt{Y}} \right\rangle^2 \right] + \overline{\sqrt{Y}}^2 \left[\left\langle \widetilde{\sqrt{X}}^2 \right\rangle - \left\langle \widetilde{\sqrt{X}} \right\rangle^2 \right] + 2\overline{\sqrt{X}\sqrt{Y}} \left\langle \widetilde{\sqrt{X}}\widetilde{\sqrt{Y}} \right\rangle \\
&= \bar{X}\mathrm{Var}(\sqrt{Y}) + \bar{Y}\mathrm{Var}(\sqrt{X}) + 2\overline{\sqrt{X}\sqrt{Y}}\mathrm{Cov}(\sqrt{X}, \sqrt{Y}) \\
&= \frac{\bar{X}}{4\bar{Y}}\mathrm{Var}(Y) + \frac{\bar{Y}}{4\bar{X}}\mathrm{Var}(X) + 2\mathrm{Cov}(X, Y)
\end{aligned} \tag{5.11}$$

Finally, we can treat $\left[\left\langle Z\sqrt{X}\sqrt{Y} \right\rangle - \langle Z \rangle \left\langle \sqrt{X}\sqrt{Y} \right\rangle \right]$ using the same substituted variables $\overline{\sqrt{X}}, \overline{\sqrt{Y}}, \widetilde{\sqrt{X}}$, and $\widetilde{\sqrt{Y}}$ and again using the fact that all of $\tilde{X}, \tilde{Y}$, and $\tilde{Z}$ have 0 mean. To be consistent with the approximations used to obtain 5.11, we will also

drop the term that is degree 3 in error.

$$\begin{aligned}
&\left\langle Z\sqrt{X}\sqrt{Y}\right\rangle - \langle Z\rangle\left\langle\sqrt{X}\sqrt{Y}\right\rangle \\
&= \left\langle (\bar{Z}+\tilde{Z})\left(\overline{\sqrt{X}}+\widetilde{\sqrt{X}}\right)\left(\overline{\sqrt{Y}}+\widetilde{\sqrt{Y}}\right)\right\rangle - \bar{Z}\left\langle\left(\overline{\sqrt{X}}+\widetilde{\sqrt{X}}\right)\left(\overline{\sqrt{Y}}+\widetilde{\sqrt{Y}}\right)\right\rangle \\
&= \overline{\sqrt{X}}\mathrm{Cov}(Z,\sqrt{Y}) + \overline{\sqrt{Y}}\mathrm{Cov}(Z,\sqrt{X}) \\
&= \frac{\sqrt{\overline{X}}}{2\sqrt{\bar{Y}}}\mathrm{Cov}(Z,Y) + \frac{\sqrt{\overline{Y}}}{2\sqrt{\bar{X}}}\mathrm{Cov}(Z,X)
\end{aligned} \tag{5.12}$$

The final result of these calculations is that the variance of the entanglement bound for a given bipartition over M samples is:

$$\begin{aligned}
\mathrm{Var}(G) = \mathrm{Var}(Z) &+ \frac{\overline{X}}{4\overline{Y}}\mathrm{Var}(Y) + \frac{\overline{Y}}{4\overline{X}}\mathrm{Var}(X) \\
&+ 2\mathrm{Cov}\left(X,Y\right) - \frac{\sqrt{\overline{X}}}{\overline{Y}}\mathrm{Cov}\left(Z,Y\right) - \frac{\sqrt{\overline{Y}}}{\overline{X}}\mathrm{Cov}\left(Z,X\right)
\end{aligned} \tag{5.13}$$

5.3.5 Total Error

Combining the random and systematic errors obtained from analysis both within and beyond a measurement period, we obtain a total uncertainty in G, ΔG:

$$\Delta G = \sqrt{\mathrm{Var}(G)} + \delta G \times \langle G\rangle \tag{5.14}$$

Chapter 6

Conclusion

In this thesis we presented measurements of genuine tripartite entanglement from photon triplets resulting from 3-photon SPDC as well as characterization of the TWPA used to measure them.

In chapter 2, the fundamentals of superconducting circuits were presented along with some of the device design of the parametric cavity and a derivation of its driven cubic Hamiltonian used to perform 3-photon SPDC.

In chapter 3, the methodology for creating a low-temperature and low-noise environment in which these states can be generated was discussed along with methodology for measuring them. Theory and application of parametric amplifiers was covered with a focus on unique considerations for use of TWPAs. Operation of an SNTJ for absolute measurements of gain, physical temperature, and noise temperature in a cryogenic environment was covered along with methodology for characterizing the gain and noise temperature of an amplifier under test. Finally, the first measurements of the noise temperature of a QuantWare TWPA were presented with findings of only around half a photon of noise above the quantum limit over its lower gain band. Furthermore, the cryogenic microwave networks used to characterize the QuantWare TWPA and to perform the 3-photon SPDC discussed later were presented.

In chapter 4, the theory of obtaining expectations of quantum operators from statistics of linear measurements made on amplified signals was presented. A description of the amplification process in terms of quantum field operators was given along with methodology for inferring the expectations of only the input signal using ON and OFF measurements. Furthermore the relationship between single-mode field operators discussed in theory and the continuum operators that more physically describe

our propagating states was elucidated. Separately, the properties of entanglement for Gaussian and non-Gaussian states was discussed as well as the importance of non-Gaussian states for various quantum information applications. Finally, a non-Gaussian entanglement condition for genuine tripartite entanglement was derived.

In chapter 5, tuneup of the parametric cavity and the measurement apparatus was discussed and novel measurements of the genuine tripartite entanglement of photon triplets from 3-photon SPDC are presented. Under a tuned parametric drive, the value of the entanglement witness derived in chapter 4 was found to be $G = 0.054 \pm 0.003$ violating the entanglement condition by over 15 sigmas. Furthermore, we measured this witness while varying the power of the parametric drive and found violation of the inequality for a range of powers over an order of magnitude. Finally, we presented an error analysis on the measurements of the entanglement witness used to obtain the uncertainty stated above.

6.1 Future Work

While entanglement of photon triplets from 3-photon SPDC was observed, its usefulness for applications like quantum sensing or quantum metrology have not yet been demonstrated. Quantum Fisher information is one method for quantifying metrological usefulness while recent theoretical work has proposed methods for computing the quantum Fisher information of photon triplets for a multimode parameter-estimation measurement [54]. These measurements rely on moments of field quadratures and should be experimentally feasible with the same device and measurement apparatus used.

Moreover, 3-photon SPDC into a single mode yields a similar non-Gaussianity as in the case of the SPDC into three distinguishable frequency modes which brings with it its own interesting properties [55]. Experiments have been performed observing Wigner negativity in these states and producing cubic phase states using a variant of this cubic Hamiltonian [10]. These non-Gaussian states known to be a resource for quantum information applications and performing carefully selected Gaussian operations on them within the parametric cavity could enable the demonstration of interesting communication or computation protocols.

Bibliography

[1] Y. Kim, A. Eddins, S. Anand, K. X. Wei, E. van den Berg, S. Rosenblatt, H. Nayfeh, Y. Wu, M. Zaletel, K. Temme, and A. Kandala, "Evidence for the utility of quantum computing before fault tolerance," *Nature*, vol. 618, pp. 500–505, Jun 2023.

[2] L. S. Madsen, F. Laudenbach, M. F. Askarani, F. Rortais, T. Vincent, J. F. F. Bulmer, F. M. Miatto, L. Neuhaus, L. G. Helt, M. J. Collins, A. E. Lita, T. Gerrits, S. W. Nam, V. D. Vaidya, M. Menotti, I. Dhand, Z. Vernon, N. Quesada, and J. Lavoie, "Quantum computational advantage with a programmable photonic processor," *Nature*, vol. 606, pp. 75–81, Jun 2022.

[3] B. Ndagano, H. Defienne, D. Branford, Y. D. Shah, A. Lyons, N. Westerberg, E. M. Gauger, and D. Faccio, "Quantum microscopy based on hong–ou–mandel interference," *Nature Photonics*, vol. 16, pp. 384–389, May 2022.

[4] R. C. Farrell, M. Illa, A. N. Ciavarella, and M. J. Savage, "Quantum simulations of hadron dynamics in the schwinger model using 112 qubits," *Phys. Rev. D*, vol. 109, p. 114510, Jun 2024.

[5] W. Wang, Y. Wu, Y. Ma, W. Cai, L. Hu, X. Mu, Y. Xu, Z.-J. Chen, H. Wang, Y. P. Song, H. Yuan, C.-L. Zou, L.-M. Duan, and L. Sun, "Heisenberg-limited single-mode quantum metrology in a superconducting circuit," *Nature Communications*, vol. 10, p. 4382, Sep 2019.

[6] I.-C. Hoi, T. Palomaki, J. Lindkvist, G. Johansson, P. Delsing, and C. M. Wilson, "Generation of nonclassical microwave states using an artificial atom in 1d open space," *Phys. Rev. Lett.*, vol. 108, p. 263601, Jun 2012.

[7] C. Eichler, D. Bozyigit, C. Lang, L. Steffen, J. Fink, and A. Wallraff, "Experimental state tomography of itinerant single microwave photons," *Phys. Rev. Lett.*, vol. 106, p. 220503, Jun 2011.

[8] C. M. Wilson, G. Johansson, A. Pourkabirian, M. Simoen, J. R. Johansson, T. Duty, F. Nori, and P. Delsing, "Observation of the dynamical casimir effect in a superconducting circuit," *Nature*, vol. 479, pp. 376–379, Nov 2011.

[9] P. Campagne-Ibarcq, A. Eickbusch, S. Touzard, E. Zalys-Geller, N. E. Frattini, V. V. Sivak, P. Reinhold, S. Puri, S. Shankar, R. J. Schoelkopf, L. Frunzio, M. Mirrahimi, and M. H. Devoret, "Quantum error correction of a qubit encoded in grid states of an oscillator," *Nature*, vol. 584, pp. 368–372, Aug 2020.

[10] A. M. Eriksson, T. Sépulcre, M. Kervinen, T. Hillmann, M. Kudra, S. Dupouy, Y. Lu, M. Khanahmadi, J. Yang, C. Castillo-Moreno, P. Delsing, and S. Gasparinetti, "Universal control of a bosonic mode via drive-activated native cubic interactions," *Nature Communications*, vol. 15, p. 2512, Mar 2024.

[11] J. Bardeen, L. N. Cooper, and J. R. Schrieffer, "Theory of superconductivity," *Phys. Rev.*, vol. 108, pp. 1175–1204, Dec 1957.

[12] M. Tinkham, *Introduction to Superconductivity*. Dover Books on Physics Series, Dover Publications, 2004.

[13] R. Gross and A. Marx, "Applied superconductivity: Josephson effect and superconducting electronics," October 2005.

[14] W. Meissner and R. Ochsenfeld, "Ein neuer effekt bei eintritt der supraleitfähigkeit," *Naturwissenschaften*, vol. 21, pp. 787–788, Nov 1933.

[15] F. London, H. London, and F. A. Lindemann, "The electromagnetic equations of the supraconductor," *Proceedings of the Royal Society of London. Series A - Mathematical and Physical Sciences*, vol. 149, no. 866, pp. 71–88, 1935.

[16] G. J. Dolan, "Offset masks for lift-off photoprocessing," *Applied Physics Letters*, vol. 31, pp. 337–339, 09 1977.

[17] B. Josephson, "Possible new effects in superconductive tunnelling," *Physics Letters*, vol. 1, no. 7, pp. 251–253, 1962.

[18] J. Koch, T. M. Yu, J. Gambetta, A. A. Houck, D. I. Schuster, J. Majer, A. Blais, M. H. Devoret, S. M. Girvin, and R. J. Schoelkopf, "Charge-insensitive qubit design derived from the cooper pair box," *Phys. Rev. A*, vol. 76, p. 042319, Oct 2007.

[19] J. Clarke and R. H. Koch, "The impact of high-temperature superconductivity on squid magnetometers," *Science*, vol. 242, no. 4876, pp. 217–223, 1988.

[20] H. Mabuchi and A. C. Doherty, "Cavity quantum electrodynamics: Coherence in context," *Science*, vol. 298, no. 5597, pp. 1372–1377, 2002.

[21] H. Paik, D. I. Schuster, L. S. Bishop, G. Kirchmair, G. Catelani, A. P. Sears, B. R. Johnson, M. J. Reagor, L. Frunzio, L. I. Glazman, S. M. Girvin, M. H. Devoret, and R. J. Schoelkopf, "Observation of high coherence in josephson junction qubits measured in a three-dimensional circuit qed architecture," *Phys. Rev. Lett.*, vol. 107, p. 240501, Dec 2011.

[22] "Ieee standard letter designations for radar-frequency bands," *IEEE Std 521-2019 (Revision of IEEE Std 521-2002)*, pp. 1–15, 2020.

[23] C. Wen, "Coplanar waveguide: A surface strip transmission line suitable for nonreciprocal gyromagnetic device applications," *IEEE Transactions on Microwave Theory and Techniques*, vol. 17, no. 12, pp. 1087–1090, 1969.

[24] D. Pozar, *Microwave Engineering*. Wiley, 2011.

[25] K. M. Sundqvist, S. Kintaş, M. Simoen, P. Krantz, M. Sandberg, C. M. Wilson, and P. Delsing, "The pumpistor: A linearized model of a flux-pumped superconducting quantum interference device for use as a negative-resistance parametric amplifier," *Applied Physics Letters*, vol. 103, p. 102603, 09 2013.

[26] A. Blais, A. L. Grimsmo, S. M. Girvin, and A. Wallraff, "Circuit quantum electrodynamics," *Rev. Mod. Phys.*, vol. 93, p. 025005, May 2021.

[27] C. W. S. Chang, C. Sabín, P. Forn-Díaz, F. Quijandría, A. M. Vadiraj, I. Nsanzineza, G. Johansson, and C. M. Wilson, "Observation of three-photon spontaneous parametric down-conversion in a superconducting parametric cavity," *Phys. Rev. X*, vol. 10, p. 011011, Jan 2020.

[28] C. M. Caves, "Quantum limits on noise in linear amplifiers," *Phys. Rev. D*, vol. 26, pp. 1817–1839, Oct 1982.

[29] C. M. Caves, J. Combes, Z. Jiang, and S. Pandey, "Quantum limits on phase-preserving linear amplifiers," *Phys. Rev. A*, vol. 86, p. 063802, Dec 2012.

[30] M. Simoen, C. W. S. Chang, P. Krantz, J. Bylander, W. Wustmann, V. Shumeiko, P. Delsing, and C. M. Wilson, "Characterization of a multimode coplanar waveguide parametric amplifier," *Journal of Applied Physics*, vol. 118, Oct. 2015.

[31] K. O'Brien, C. Macklin, I. Siddiqi, and X. Zhang, "Resonant phase matching of josephson junction traveling wave parametric amplifiers," *Phys. Rev. Lett.*, vol. 113, p. 157001, Oct 2014.

[32] C. Macklin, K. O'Brien, D. Hover, M. E. Schwartz, V. Bolkhovsky, X. Zhang, W. D. Oliver, and I. Siddiqi, "A near–quantum-limited josephson traveling-wave parametric amplifier," *Science*, vol. 350, no. 6258, pp. 307–310, 2015.

[33] M. V. Moghaddam, C. W. S. Chang, I. Nsanzineza, A. M. Vadiraj, and C. M. Wilson, "Carbon nanotube-based lossy transmission line filter for superconducting qubit measurements," *Applied Physics Letters*, vol. 115, p. 213504, 11 2019.

[34] L. Spietz, K. W. Lehnert, I. Siddiqi, and R. J. Schoelkopf, "Primary electronic thermometry using the shot noise of a tunnel junction," *Science*, vol. 300, no. 5627, pp. 1929–1932, 2003.

[35] S.-W. Chang, J. Aumentado, W.-T. Wong, and J. C. Bardin, "Noise measurement of cryogenic low noise amplifiers using a tunnel-junction shot-noise source," in *2016 IEEE MTT-S International Microwave Symposium (IMS)*, pp. 1–4, 2016.

[36] M. Malnou, T. F. Q. Larson, J. D. Teufel, F. Lecocq, and J. Aumentado, "Low-noise cryogenic microwave amplifier characterization with a calibrated noise source," *Review of Scientific Instruments*, vol. 95, p. 034703, 03 2024.

[37] L. Spietz, R. J. Schoelkopf, and P. Pari, "Shot noise thermometry down to 10mK," *Applied Physics Letters*, vol. 89, p. 183123, 11 2006.

[38] C. Weedbrook, S. Pirandola, R. García-Patrón, N. J. Cerf, T. C. Ralph, J. H. Shapiro, and S. Lloyd, "Gaussian quantum information," *Rev. Mod. Phys.*, vol. 84, pp. 621–669, May 2012.

[39] C. Eichler, D. Bozyigit, and A. Wallraff, "Characterizing quantum microwave radiation and its entanglement with superconducting qubits using linear detectors," *Phys. Rev. A*, vol. 86, p. 032106, Sep 2012.

[40] M. P. da Silva, D. Bozyigit, A. Wallraff, and A. Blais, "Schemes for the observation of photon correlation functions in circuit qed with linear detectors," *Phys. Rev. A*, vol. 82, p. 043804, Oct 2010.

[41] B. Yurke and J. S. Denker, "Quantum network theory," *Phys. Rev. A*, vol. 29, pp. 1419–1437, Mar 1984.

[42] R. Loudon, *The Quantum Theory of Light*. Oxford science publications, Clarendon Press, 1983.

[43] K. J. Blow, R. Loudon, S. J. D. Phoenix, and T. J. Shepherd, "Continuum fields in quantum optics," *Phys. Rev. A*, vol. 42, pp. 4102–4114, Oct 1990.

[44] M. Walschaers, "Non-gaussian quantum states and where to find them," *PRX Quantum*, vol. 2, p. 030204, Sep 2021.

[45] C. W. Sandbo Chang, M. Simoen, J. Aumentado, C. Sabín, P. Forn-Díaz, A. M. Vadiraj, F. Quijandría, G. Johansson, I. Fuentes, and C. M. Wilson, "Generating multimode entangled microwaves with a superconducting parametric cavity," *Phys. Rev. Appl.*, vol. 10, p. 044019, Oct 2018.

[46] L. K. Shalm, D. R. Hamel, Z. Yan, C. Simon, K. J. Resch, and T. Jennewein, "Three-photon energy–time entanglement," *Nature Physics*, vol. 9, p. 19–22, Nov. 2012.

[47] P. van Loock and A. Furusawa, "Detecting genuine multipartite continuous-variable entanglement," *Phys. Rev. A*, vol. 67, p. 052315, May 2003.

[48] R. Y. Teh and M. D. Reid, "Criteria for genuine n-partite continuous-variable entanglement and einstein-podolsky-rosen steering," *Phys. Rev. A*, vol. 90, p. 062337, Dec 2014.

[49] H. Yonezawa, T. Aoki, and A. Furusawa, "Demonstration of a quantum teleportation network for continuous variables," *Nature*, vol. 431, pp. 430–433, Sep 2004.

[50] H. Strobel, W. Muessel, D. Linnemann, T. Zibold, D. B. Hume, L. Pezzè, A. Smerzi, and M. K. Oberthaler, "Fisher information and entanglement of non-gaussian spin states," *Science*, vol. 345, no. 6195, pp. 424–427, 2014.

[51] E. A. R. González, A. Borne, B. Boulanger, J. A. Levenson, and K. Bencheikh, "Continuous-variable triple-photon states quantum entanglement," *Phys. Rev. Lett.*, vol. 120, p. 043601, Jan 2018.

[52] M. Hillery, H. T. Dung, and H. Zheng, "Conditions for entanglement in multipartite systems," *Phys. Rev. A*, vol. 81, p. 062322, Jun 2010.

[53] A. Agustí, C. W. S. Chang, F. Quijandría, G. Johansson, C. M. Wilson, and C. Sabín, "Tripartite genuine non-gaussian entanglement in three-mode spontaneous parametric down-conversion," *Phys. Rev. Lett.*, vol. 125, p. 020502, Jul 2020.

[54] M. Tian, Y. Xiang, F.-X. Sun, M. Fadel, and Q. He, "Characterizing multipartite non-gaussian entanglement for a three-mode spontaneous parametric down-conversion process," *Phys. Rev. Appl.*, vol. 18, p. 024065, Aug 2022.

[55] Y. Zheng, O. Hahn, P. Stadler, P. Holmvall, F. Quijandría, A. Ferraro, and G. Ferrini, "Gaussian conversion protocols for cubic phase state generation," *PRX Quantum*, vol. 2, p. 010327, Feb 2021.

APPENDICES

Appendix A

State Moments From Measurements

The general approach to obtaining the moments of the cavity output from ON and OFF subtraction is to recognize that odd moments of Gaussian noise from the amplification chain must all be 0 valued. Furthermore, since the Gaussian noise is delta correlated in time, its operators at different mode frequencies should also be entirely independent. In reality, we recognize that there is a multiplicative random variable on each moment due to drift in the gain of the amplification chain which creates some correlations between moments. However, since this drift is multiplicative and uncorrelated with the propagating state, it only creates nonzero correlations between operations that have nonzero mean or are already correlated. This can be seen for some arbitrary operators $\hat{A}, \hat{B}$ that are then multiplied by $\text{Gain}_A, \text{Gain}_B$ respectively:

$$\langle(\text{Gain}_A\hat{A})(\text{Gain}_B\hat{B})\rangle = \langle\text{Gain}_A\text{Gain}_B\rangle\langle\hat{A}\hat{B}\rangle \tag{A.1}$$

Which is still 0 if $\langle\hat{A}\hat{B}\rangle = 0$. Just like in chapter 4.2, we will use the subscript ρ to denote moments of the signal with the parametric pump ON and the subscript $|0\rangle\langle 0|$ to denote moments of the signal with the parametric pump OFF.

A.1 $\langle \hat{a} \rangle$

$$\begin{aligned} \langle \hat{S} \rangle_\rho &= \langle \hat{a} \rangle + \langle \hat{h}^\dagger \rangle \\ &= \langle \hat{a} \rangle \\ \langle \hat{S} \rangle_{|0\rangle\langle 0|} &= 0 + \langle \hat{h}^\dagger \rangle \end{aligned}$$

$$\therefore \langle \hat{a} \rangle = \langle \hat{S} \rangle_\rho \tag{A.2}$$

A.2 $\langle \hat{a}^\dagger \rangle$

$$\langle \hat{a}^\dagger \rangle = \langle \hat{S}^\dagger \rangle_\rho \tag{A.3}$$

A.3 $\langle \hat{a}^\dagger \hat{a} \rangle$

This operator is of course the number operator, $\langle \hat{a}^\dagger \hat{a} \rangle = \langle \hat{N}_a \rangle$.

$$\begin{aligned} \langle \hat{S}^\dagger \hat{S} \rangle_\rho &= \langle \hat{N}_a \rangle + \langle \hat{a} \hat{h}^\dagger \rangle + \langle \hat{a}^\dagger \hat{h} \rangle + \langle \hat{h} \hat{h}^\dagger \rangle \\ &= \langle \hat{N}_a \rangle + \langle \hat{a} \rangle \langle \hat{h}^\dagger \rangle + \langle \hat{a}^\dagger \rangle \langle \hat{h} \rangle + \langle \hat{h} \hat{h}^\dagger \rangle \\ &= \langle \hat{N}_a \rangle + \langle \hat{h} \hat{h}^\dagger \rangle \\ \langle \hat{S}^\dagger \hat{S} \rangle_{|0\rangle\langle 0|} &= 0 + \langle \hat{h} \hat{h}^\dagger \rangle \end{aligned}$$

$$\therefore \langle \hat{N}_a \rangle = \langle \hat{S}^\dagger \hat{S} \rangle_\rho - \langle \hat{S}^\dagger \hat{S} \rangle_{|0\rangle\langle 0|} \tag{A.4}$$

A.4 $\langle \hat{a}^\dagger \hat{a} \hat{b}^\dagger \hat{b} \rangle$

Similarly, we can also write $\langle \hat{a}^\dagger \hat{a} \hat{b}^\dagger \hat{b} \rangle = \langle \hat{N}_a \hat{N}_b \rangle$. We can also permute this over any pair of $\hat{a}, \hat{b}, \hat{c}$. For cleanliness going forward we will preemptively drop any terms containing odd numbers of noise moments $\langle \hat{h} \rangle$, $\langle \hat{h}^\dagger \rangle$ for any single mode as we know

that they will equal 0.

$$\begin{aligned}\langle \hat{S}_a^\dagger \hat{S}_a \hat{S}_b^\dagger \hat{S}_b \rangle_\rho &= \langle \hat{N}_a \hat{N}_b \rangle + \langle \hat{N}_a \rangle \langle \hat{h}_b^\dagger \hat{h}_b \rangle + \langle \hat{N}_b \rangle \langle \hat{h}_a^\dagger \hat{h}_a \rangle + \langle \hat{h}_a^\dagger \hat{h}_a \hat{h}_b^\dagger \hat{h}_b \rangle \\ \langle \hat{S}_a^\dagger \hat{S}_a \hat{S}_b^\dagger \hat{S}_b \rangle_{|0\rangle\langle 0|} &= 0 + 0 + 0 + \langle \hat{h}_a^\dagger \hat{h}_a \hat{h}_b^\dagger \hat{h}_b \rangle \end{aligned}$$

$$\begin{aligned}\therefore \langle \hat{N}_a \hat{N}_b \rangle &= \langle \hat{S}_a^\dagger \hat{S}_a \hat{S}_b^\dagger \hat{S}_b \rangle_\rho - \langle \hat{N}_a \rangle \langle \hat{S}_b^\dagger \hat{S}_b \rangle_{|0\rangle\langle 0|} \\ &\quad - \langle \hat{N}_b \rangle \langle \hat{S}_a^\dagger \hat{S}_a \rangle_{|0\rangle\langle 0|} - \langle \hat{S}_a^\dagger \hat{S}_a \hat{S}_b^\dagger \hat{S}_b \rangle_{|0\rangle\langle 0|} \end{aligned} \tag{A.5}$$

A.5 $\langle \hat{a}\hat{b}\hat{c} \rangle$

$$\begin{aligned}\langle \hat{S}_a \hat{S}_b \hat{S}_c \rangle_\rho &= \langle \hat{a}\hat{b}\hat{c} \rangle \\ \therefore \langle \hat{a}\hat{b}\hat{c} \rangle &= \langle \hat{S}_a \hat{S}_b \hat{S}_c \rangle_\rho \end{aligned} \tag{A.6}$$